Metabolically controlled histone H4K5 acylation/acetylation ratio drives BRD4 genomic distribution

Mengqing Gao, Jin Wang, Sophie Rousseaux, Minjia Tan, Lulu Pan, Lijun Peng, Sisi Wang, Wenqian Xu, Jiayi Ren, Yuanfang Liu, et al.

Cell Reports

Article

Metabolically controlled histone H4K5 acylation/acetylation ratio drives BRD4 genomic distribution

Graphical abstract

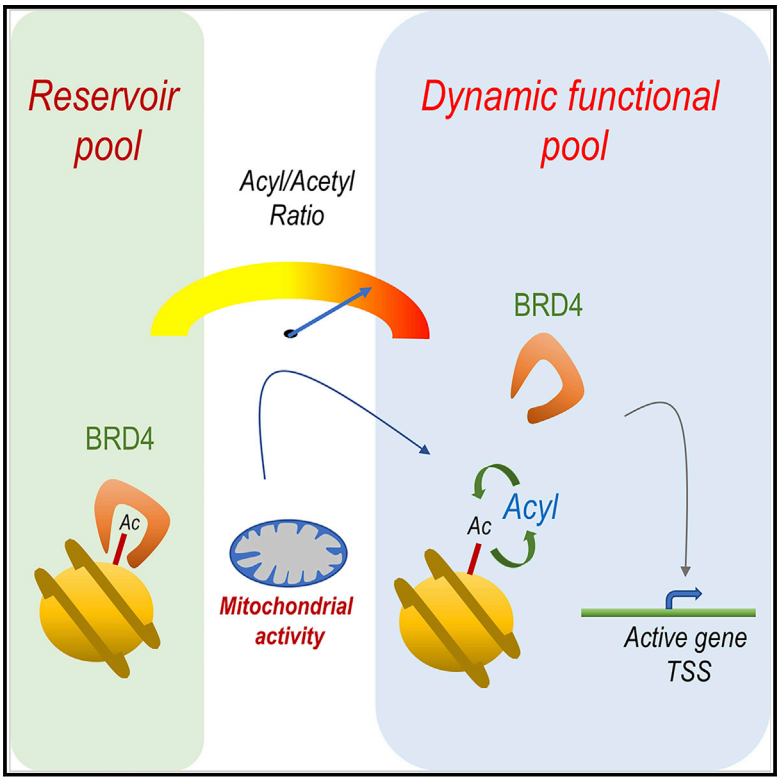

Authors

Mengqing Gao, Jin Wang, Sophie Rousseaux, ..., Yingming Zhao, Jian-Qing Mi, Saadi Khochbin

Correspondence

jianqingmi@shsmu.edu.cn (J.-Q.M.), saadi.khochbin@univ-grenoble-alpes.fr (S.K.)

In brief

Gao et al. show that metabolically driven dynamic exchange between acylations and acetylation on histone H4K5 defines the stability of BRD4 interactions with chromatin. A high H4K5 acylation/acetylation ratio loosens BRD4 from its chromatin binding sites, increasing the pool of available BRD4 for recruitment on active TSS regions and transcriptional regulation.

Highlights

- Mitochondrial activity controls H4K5 acylation/acetylation ratio
- H4K5 acylation/acetylation ratio fine-tunes BRD4-chromatin interactions
- H4K5 acylation/acetylation ratio regulates BRD4 reservoir and functional pools
- H4K5 non-acetyl acylations could be considered a single functional entity

Gao et al., 2021, Cell Reports *36*, 109460
July 27, 2021
https://doi.org/10.1016/j.celrep.2021.109460

CellPress

Cell Reports

CellPress
OPEN ACCESS

Article

Metabolically controlled histone H4K5 acylation/acetylation ratio drives BRD4 genomic distribution

Mengqing Gao,[1,2,3,10] Jin Wang,[1,3,10] Sophie Rousseaux,[2,3] Minjia Tan,[4] Lulu Pan,[4] Lijun Peng,[1,3] Sisi Wang,[1,3] Wenqian Xu,[1,3] Jiayi Ren,[1,3] Yuanfang Liu,[1] Martin Spinck,[5] Sophie Barral,[2,3] Tao Wang,[2,3] Florent Chuffart,[2,3] Ekaterina Bourova-Flin,[2,3] Denis Puthier,[6] Sandrine Curtet,[2,3] Lisa Bargier,[6] Zhongyi Cheng,[7] Heinz Neumann,[5] Jian Li,[8] Yingming Zhao,[9] Jian-Qing Mi,[1,3,*] and Saadi Khochbin[2,3,11,*]

[1]Shanghai Institute of Hematology, State Key Laboratory of Medical Genomics, National Research Center for Translational Medicine at Shanghai, Ruijin Hospital Affiliated to Shanghai Jiao Tong University School of Medicine, 200025 Shanghai, China
[2]CNRS UMR 5309/INSERM U1209/Université Grenoble-Alpes/Institute for Advanced Biosciences, 38706 La Tronche, France
[3]Pôle Franco-Chinois de Recherche en Sciences du Vivant et Génomique, 200025 Shanghai, China
[4]Shanghai Institute of Materia Medica, Chinese Academy of Sciences, 555 Zuchongzhi Road, 201203 Shanghai, China
[5]Department of Structural Biochemistry, Max Planck Institute of Molecular Physiology, Otto-Hahn-Strasse 11, 44227 Dortmund, Germany
[6]Aix Marseille Université, INSERM, TAGC, TGML, 13288 Marseille, France
[7]Jingjie PTM Biolab (Hangzhou), 310018 Hangzhou, China
[8]Clinical Research Center, Ruijin Hospital Affiliated to Shanghai Jiao Tong University School of Medicine, 200025 Shanghai, China
[9]Ben May Department of Cancer Research, The University of Chicago, Chicago, IL 60637, USA
[10]These authors contributed equally
[11]Lead contact
*Correspondence: jianqingmi@shsmu.edu.cn (J.-Q.M.), saadi.khochbin@univ-grenoble-alpes.fr (S.K.)
https://doi.org/10.1016/j.celrep.2021.109460

SUMMARY

In addition to acetylation, histones are modified by a series of competing longer-chain acylations. Most of these acylation marks are enriched and co-exist with acetylation on active gene regulatory elements. Their seemingly redundant functions hinder our understanding of histone acylations' specific roles. Here, by using an acute lymphoblastic leukemia (ALL) cell model and blasts from individuals with B-precusor ALL (B-ALL), we demonstrate a role of mitochondrial activity in controlling the histone acylation/acetylation ratio, especially at histone H4 lysine 5 (H4K5). An increase in the ratio of non-acetyl acylations (crotonylation or butyrylation) over acetylation on H4K5 weakens bromodomain containing protein 4 (BRD4) bromodomain-dependent chromatin interaction and enhances BRD4 nuclear mobility and availability for binding transcription start site regions of active genes. Our data suggest that the metabolism-driven control of the histone acetylation/longer-chain acylation(s) ratio could be a common mechanism regulating the bromodomain factors' functional genomic distribution.

INTRODUCTION

Since the discovery of histone lysine propionylation and butyrylation (Chen et al., 2007), an increasing number of different histone acylations has been reported. The vast majority of these histone post-translational modifications (PTMs) occur at sites already known to be acetylated; hence, overall, these new histone PTMs could collectively be considered acetylation-competing marks. Functional studies carried out on these histone marks in different biological systems have shown that they are associated with active genes and directly stimulate transcription, similar to histone acetylation (Dai et al., 2014; Sabari et al., 2015; Goudarzi et al., 2016; Xie et al., 2016; Kebede et al., 2017; Smestad et al., 2018; Bao et al., 2019; Huang et al., 2018; Zhang et al., 2019).

Comparative high-resolution genome mapping also revealed that, in the majority of active chromatin loci, these histone acylations co-exist with acetylation (Tan et al., 2011; Dai et al., 2014; Sabari et al., 2015; Goudarzi et al., 2016; Kebede et al., 2017; Crespo et al., 2020). Additionally, although these acylations are mostly mapped at gene transcriptional start site (TSS)-associated regions, as expected for active histone marks, their relative abundance corresponds to only a small fraction in comparison with acetylated histones (Simithy et al., 2017). Finally, although different acyl donor groups may result from different metabolic pathways, their redundant functions do not leave much room for any metabolism-specific action.

These observations therefore raise an important unsolved issue in modern biology: the specific functional significance of these histone acylations compared with acetylation.

An answer to this issue came from the discovery of specific domains in various proteins that show a better affinity for binding to longer-chain acyl groups. For instance, YEATS and DPF domains present better binding activity for crotonylated histones

than for acetylated histones (Andrews et al., 2016a; Li et al., 2016; Xiong et al., 2016).

An unexplored possibility to solve this issue is also coming from *in vitro* data showing that most bromodomains lose their affinity for chromatin regions bearing histones with acyl groups longer than three carbons (Flynn et al., 2015; Goudarzi et al., 2016; Olp et al., 2017).

The functional consequence of a differential effect of histone acylation on bromodomain-chromatin interactions was first considered in the context of the late stages of spermatogenesis, when large-scale histone hyperacetylation is coupled to genome-wide histone removal involving the testis-specific member of the bromo- and extra-terminal domain (BET) family, bromodomain testis-specific (Brdt) (Shiota et al., 2018). Using this specific system, we discovered that histone H4 bearing butyrylation at K5 and K8 (H4K5bu and H4K8bu) escapes this wave of replacement and survives longer in late spermatogenic cells than histone H4 bearing the corresponding acetylation (H4K5ac and H4K8ac). This observation supports the hypothesis that, because Brdt's first bromodomain is unable to bind H4 when it is modified by butyrylation specifically at K5, the corresponding histones "escape" acetylation and the subsequent Brdt-dependent removal (Goudarzi et al., 2016).

However, these observations remained correlative, and the hypothesis of modulation of the action of BET factors by an interplay between histone acetylation and acylations awaited confirmation.

Here, by taking advantage of ALL cell biology, we directly demonstrate that a modified histone acetyl/acyl ratio, specifically at H4K5, controls the dynamics of interaction between chromatin and the ubiquitously expressed member of the BET double bromodomain factor BRD4, whose expression and activity are frequently dysregulated in many unrelated cancers (Fujisawa and Filippakopoulos, 2017). The emerging general concept developed here is that a mixture of finely tuned competing histone acetylation and longer-chain acylations defines bromodomain factor functional availability.

RESULTS

Aberrant activation of Fas activated serine/threonine kinase domain 1 (*FASTKD1*) is associated with general shutdown of mitochondrial activity

We previously identified *FASTKD1* as an ectopically expressed gene in childhood and adult B-ALL (Wang et al., 2015). FASTKD1 presents a mitochondrial targeting signal and, hence, is expected to exert its function in mitochondria (Jourdain et al., 2017). To investigate its function, we first identified the established B-ALL cell line REH, expressing *FASTKD1*, and then generated REH cell lines stably expressing two different anti-*FASTKD1* short hairpin (sh) RNAs (Figure S1A) or used the CRISPR-Cas9 system to knock out the gene (Figure S1B). RNA sequencing (RNA-seq) was performed on the two *FASTKD1* knockdown as well as two independent *FASTKD1* knockout clones (Figures S1A and S1B). Focusing on mitochondrial gene expression, we observed that inactivation of *FASTKD1* leads to significant enhancement of mitochondrial gene expression (Figure 1A).

This activation of mitochondrial gene expression was also confirmed independently by qRT-PCR evaluating expression of the NADH dehydrogenase subunit 2 and subunit 3 (*ND2* and *ND3*) genes after treating cells with a series of five different anti-*FASTKD1* shRNAs as well as in the two *FASTKD1* knockout (KO) cell lines (Figure 1B, top panels; Figure S1C). Finally, FASTKD1-FLAG re-expressed in *FASTKD1* KO cells resulted in mitochondrial localization of ectopically expressed FASTKD1-FLAG and downregulation of mitochondrial gene expression (Figure S2; Figure 1B, bottom panels).

All of these data suggested that FASTKD1 should downregulate mitochondrial activity. To test this hypothesis, mitochondrial respiration was measured from control REH cells or from the two *FASTKD1* KO clones. The results show enhancement of respiration in *FASTKD1* KO clones compared with control REH cells, in perfect agreement with a role of FASTKD1 in the decrease of mitochondrial activity; more specifically, respiration (Figure 1C).

Mitochondrial activity is a driver of histone acylations

FASTKD1 appeared to us to be an excellent factor to investigate the relationship between mitochondrial activity and histone acetylation/acylation (Matilainen et al., 2017; Lozoya et al., 2019; Haws et al., 2020; Trefely et al., 2020) in the specific context of ALL. We focused on histone H3 and H4 propionylation and butyrylation because, although all bromodomains bind acetyllysines and propionyllysines, many of them are unable to bind butyryllysine (Flynn et al., 2015).

Histone extracts from wild-type REH cells and the two derived *FASTKD1* KO cell lines were used in an unbiased approach to measure changes in histone butyrylation and propionylation. After trypsin digestion of histones, the resulting peptides were directly quantified using a label-free mass spectrometry method.

These analyses were performed without prior enrichment of modified histone peptides (with anti-PTM antibodies) to detect and visualize the most abundant modified peptides.

The results demonstrated that histone H4 K5, K8, and K12 butyrylation is the most responsive to FASTKD1 depletion (Figure 2A; Tables S1–S3). A detailed analysis of the mass spectrometry data also highlighted the occurrence of unique peptides with a combination of acetylation and butyrylation-propionylation (Data S1). This observation is indicative of continuing exchanges of acylations at a particular lysine site.

We then decided to focus on H4 K5 and K8 to confirm these findings. Immunodetection of histone PTMs showed a clear increase in butyrylation and crotonylation of H4K5 and H4K8 in the two *FASTKD1* KO cell lines. The corresponding histone acetylation level did not show any noticeable change in *FASTKD1* KO cell lines (Figure 2B).

These results suggest the existence of a direct relationship between the studied histone acylations and the extent of mitochondrial activity. To confirm this conclusion, we treated control and *FASTKD1* KO cell lines with the electron transport chain poison rotenone and demonstrated that impairment of mitochondrial activity severely affects maintenance of histone H4K5 butyrylation and H4K5 crotonylation (H4K5cr) (Figure 2C). This treatment with rotenone had relatively little effect on acetylation, probably because of the considerably higher levels and more stable pools of acetyl-coenzyme A (CoA) and acetylated histones.

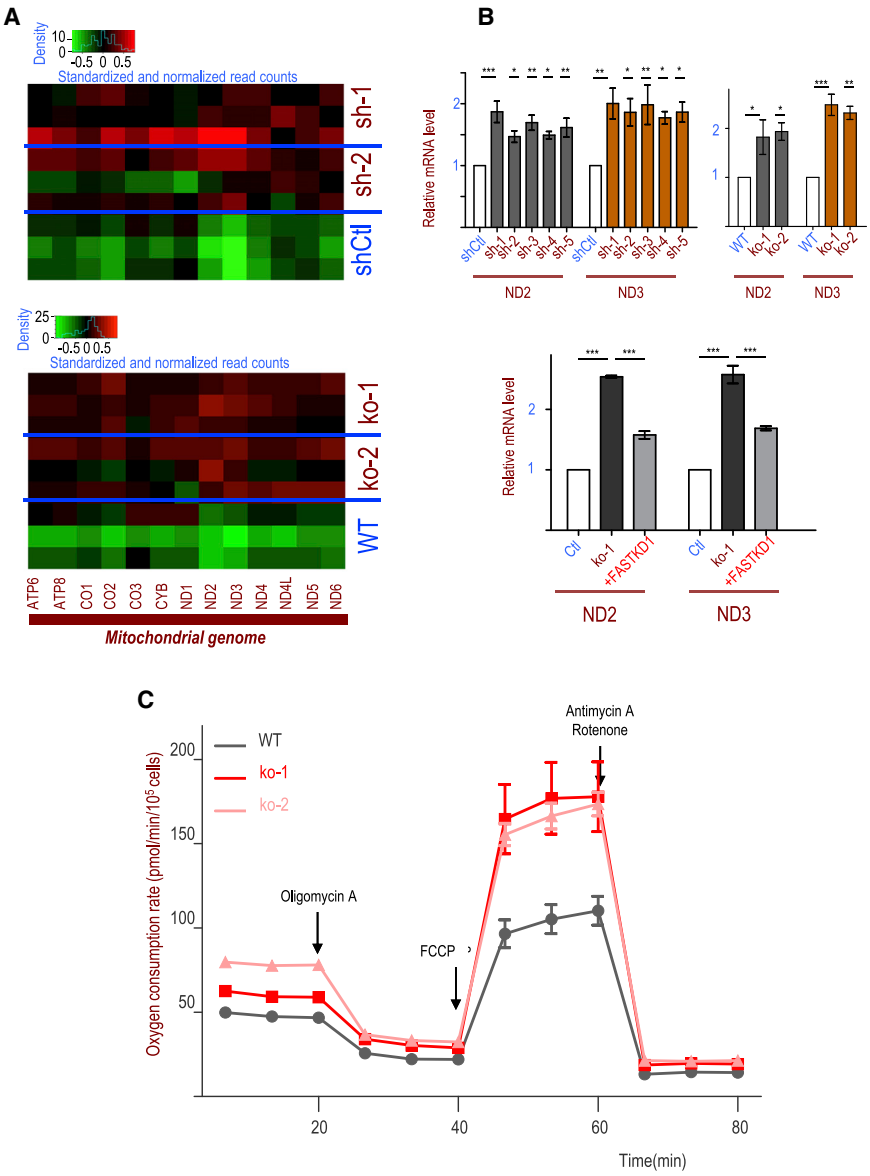

Figure 1. FASTKD1 controls mitochondrial activity

(A) Total RNAs from REH cells stably expressing two independent anti-*FASTKD1* shRNAs (sh-1 and sh-2) or bearing inactivation of *FASTKD1* gene (KO-1 and KO-2) were sequenced, and the standardized and normalized read counts representing mitochondrial gene expression under the different conditions are shown on a heatmap.

(B) Expression of the *ND2* and *ND3* genes encoded by the mitochondrial genome was monitored by qRT-PCR in REH cells stably expressing empty vector (shCtl) or five independent anti-*FASTKD1* shRNAs (top left panel). The expression of *ND2* and *ND3* was also monitored by qRT-PCR in wild-type and the two *FASTKD1* KO REH cells (top right panel). *FASTKD1* KO-1 cells were used to re-express *FASTKD1-FLAG*, and expression of *ND2* and *ND3* was monitored by qRT-PCR in wild-type, KO-1, and *FASTKD1* rescued cells (bottom panel). Fold changes of gene expression levels were calculated via the delta-delta-Ct (2^{-}-ddCt) algorithm and are represented by mean ± standard error of the mean (SEM) based on at least three independent experiments. Statistical differences between wild-type and two *KO* or between shCtl and shRNAs groups were calculated with Fisher's least significant difference (LSD) after one-way ANOVA test. *p < 0.05, **p < 0.01, ***p < 0.001.

(C) Wild-type and the two *FASTKD1* KO REH clones were assayed for respiration capacity using the standard Seahorse Mito Stress assay. The data shown are the mean value ± SEM of 5 biological replicate measurements.

See Figure S1 for information regarding generation of REH knockdown and KO cells. See Figure S2 for mitochondrial targeting of FASTKD1.

Fatty acid synthesis/β-oxidation is a major driver of histone butyrylation and crotonylation

Fatty acid synthesis and β-oxidation particularly involve generation of acyl-CoA derivatives that could potentially contribute to histone acylations (Pougovkina et al., 2014; McDonnell et al., 2016; Gowans et al., 2019; Tarazona and Pourquié, 2020). We therefore first used a competitive inhibitor of acyl-CoA synthetase, Triascin C, to prevent synthesis of fatty acids and monitored the effect on H4K5K8 acetylation and butyrylation (Figure 2H, scheme). Treatment of cells with triascin C abolished the increase in H4 butyrylation at H4K5 observed in *FASTKD1* KO lines, with no remarkable effect on acetylation of this residue (Figure 2D). Additionally, we decided to target the enzyme that catalyzes the first step of fatty acid synthesis, acetyl-CoA carboxylase (ACC1; Figure 2H, scheme), by using the ACC1 inhibitor ND-630. Inhibition of ACC1 also abolished the increased level of H4K5bu compared with the parental cells, with no remarkable effect on acetylation of H4 lysine 5 (H4K5ac) (Figure 2E).

To also test the role of fatty acid oxidation (FAO) in histone acylations, we treated the cells with octanoate, a molecule directly usable in FAO (McDonnell et al., 2016). Octanoate treatment increases the levels of H4K5 acetylation, butyrylation, and crotonylation in REH cells (Figure 2F; Figure S3). However, compared with acetylation, the increase in H4K5bu-cr is more remarkable (Figure S3).

To further test the role of FAO in histone acylation, we also used ranolazine, an inhibitor of FAO, and showed that treatment of cells with this inhibitor abolishes the increase in H4K5bu observed in the *FASTKD1* KO clones (Figure 2G).

β-Oxidation and mitochondrial activity are major sources of histone acylation in ALL malignancies

To generalize our conclusions regarding the relationship between mitochondrial activity and histone acylations, we quantitatively measured H4K5cr and H4K5bu by ELISA in 31 B-ALL cell

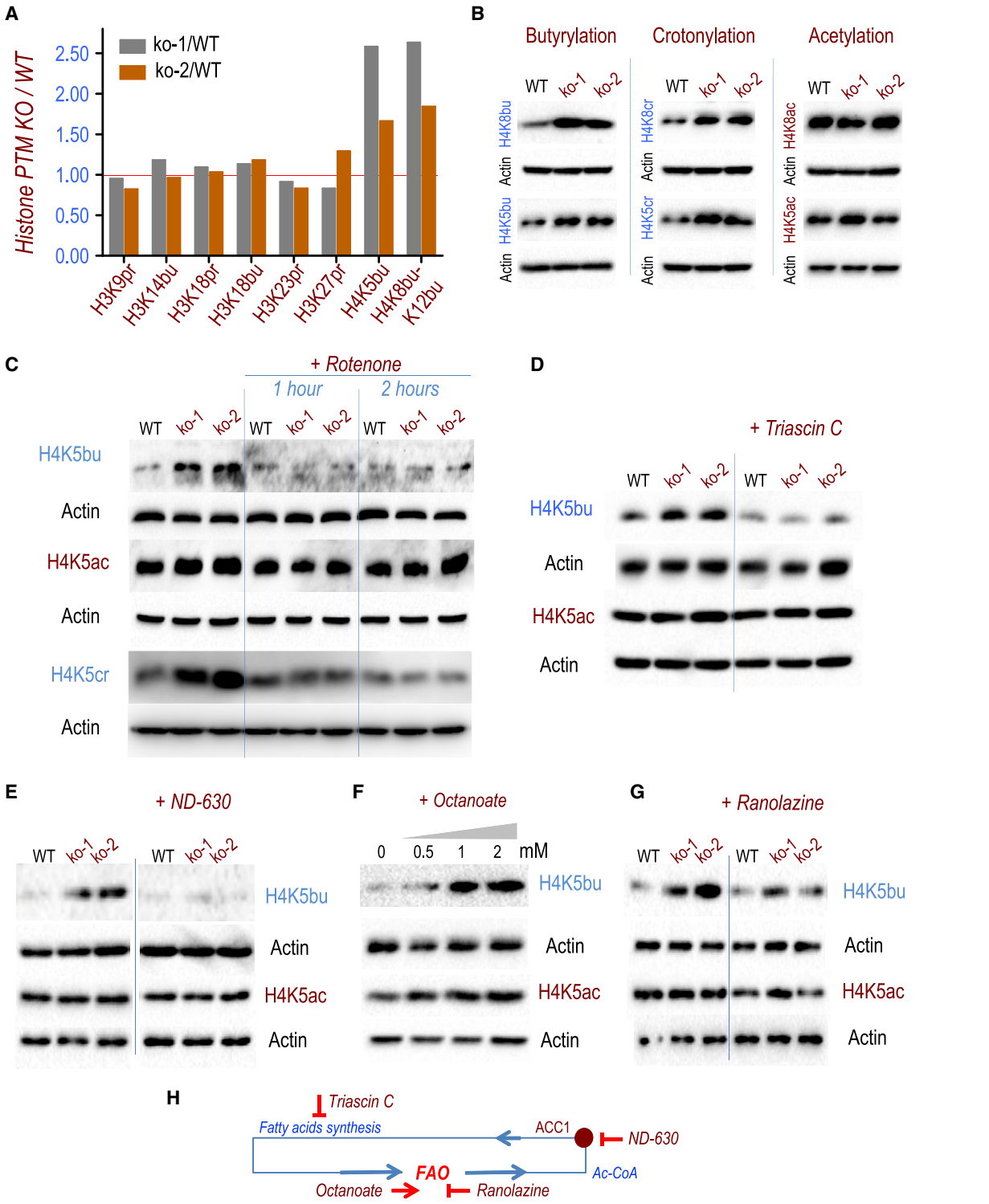

Figure 2. *FASTKD1* gene inactivation, mitochondrial activation, and β-oxidation lead to an increase in H4K5K8 acylations

(A) Histone extracts from wild-type and *FASTKD1* KO cells were analyzed by label-free mass spectrometry. The relative abundance of the indicated identified site-specific modifications was determined and expressed as the ratio of *FASTKD1* KO to the wild type. The core histone peptides were used to normalize the corresponding modified peptides. H4K8bu- and H4K12bu-containing peptides could not be distinguished following these analyses. Consequently, the quantification regarding these two modification sites was plotted as H4K8bu-K12bu.

(legend continued on next page)

samples from affected individuals (Table S4). Using qRT-PCR in the same samples, we quantified carnitine palmitoyltransferase 1A (*CPT1A*) mRNA, encoding a protein involved in the transport of long-chain acyl groups into mitochondria and in controlling the fatty acids β-oxidation potential of the cells, as well as the mitochondrial gene *ND2* mRNA as an indicator of mitochondrial activity.

Figure 3A shows that there is a tendency for coregulation between the expression of *CPT1A* mRNA as a measure of β-oxidation potential and the expression level of *ND2* as a measure of mitochondrial activity (Spearman's rank [sr] correlation coefficient = 0.531).

From our functional data obtained in REH cells (Figures 1 and 2), we expected to find a relationship between the level of mitochondrial transcription (*ND2* mRNA) and the intensity of H4K5 crotonylation and butyrylation. To test this hypothesis, ALL samples were divided into two groups as a function of the expression of *ND2*. A Receiver Operating Characteristic (ROC) curve of the qRT-PCR output values was used to define a cutoff value at −dCt = 1.2782, which we used to stratify the ALL into two groups of 13 (42%) low-*ND2*-expressing and 18 (58%) high-*ND2*-expressing samples, respectively. The results showed that, similarly to REH cells, individuals' ALL cells with higher mitochondrial activity are associated with higher levels of H4K5 crotonylation and butyrylation (Figures 3B and 3C).

The H4K5 acylation/acetylation ratio is a major determinant of BRD4-chromatin interactions

In a previous study, we observed that, during late spermatogenesis, H4K5bu-containing nucleosomes escape acetylation- and Brdt-dependent histone removal (Goudarzi et al., 2016).

Our present data suggest that, similarly, in the case of ALL cells, a change in the ratio of H4K5 acetylation/butyrylation-crotonylation could also affect the interaction between BRD4 and chromatin.

Using a peptide pull-down assay with a H4 N-terminal tail peptide bearing all combinations of acetylation and butyrylation at K5 and K8, we demonstrate the inability of BRD4 to bind H4 when the peptide is modified by a butyryl group at K5 (Figure 4A). Depletion of FASTKD1 and a change in mitochondrial activity did not affect the total level of BRD4 in a high-salt nuclear extract (Figure 4B, input; see also Figure 4C) nor its ability to bind to an acetylated H4 tail peptide (Figure 4B, pull-down).

These data suggest that H4 butyrylation at H4K5 should affect the ability of BRD4 to interact with chromatin. Accordingly, an increase in H4K5bu-cr, as observed in our *FASTKD1* KO cells, should loosen, to some extent, the interaction between BRD4 and chromatin compared with wild-type cells.

To test this hypothesis, we used wild-type and *FASTKD1* KO REH cells to compare the strength of BRD4-chromatin binding with the prediction that, in *FASTKD1* KO cells, a loose BRD4-chromatin interaction should be observed because of the increase in the H4K5 acyl/acetyl ratio. Accordingly, wild-type and *FASTKD1* KO cells were lysed in a buffer containing increasing salt concentrations, and, after centrifugation, the respective amounts of BRD4 released in the supernatant or remaining bound to chromatin were visualized by immunoblotting. Figure 4C, top panels, shows that, in the presence of 200 mM NaCl, both *FASTKD1* KO clones released higher amounts of BRD4 compared with wild-type cells, suggesting weaker binding of BRD4 to chromatin.

To further support our observation, we also treated our cells with increasing concentrations of the BRD4 small-molecule inhibitor JQ1. We reasoned that a more dynamic BRD4-chromatin interaction should make BRD4 bromodomains more sensitive to inhibition by JQ1. After treating cells with solvent or 0.1, 0.5, or 5 μM of JQ1, the respective amounts of BRD4 in soluble protein extracts and in the chromatin-bound fractions were analyzed. Figure 4C, bottom panels, shows that, at 0.5 μM concentration, JQ1 treatment leads to an increase in the soluble pool of BRD4 in *FASTKD1* KO cells compared with wild-type cells.

Finally, to directly test the effect of a change in the histone acetylation/butyrylation-crotonylation ratio on the efficiency of BRD4 binding, we designed an approach to visualize a change in the dynamics of BRD4 in live cells. For this purpose, we used a previously characterized COS-7 cell-based system and induced a change in the ratio of histone acetylation/butyrylation-crotonylation in these cells. We had shown previously that expression of the oncogenic fusion protein BRD4-NUT in COS-7 cells creates well-defined nuclear foci that depend on chromatin acetylation and BRD4 bromodomains (Reynoird et al., 2010). In addition, these BRD4-NUT-induced foci are large and stable enough to allow *in vivo* approaches such as fluorescence recovery after photobleaching (FRAP) assays.

First we stably expressed CobB, a bacterial NAD^+ deacetylase designed for expression in mammalian cells (Spinck et al., 2020), in COS-7 cells and visualized the effect of this deacetylase on the acetyl/butyryl-crotonyl ratio. Figures 4D and S4A show that expression of CobB, although preferentially decreasing the level of H4K5ac, has no noticeable effect on H4K5bu and H4K5cr *in vivo* in these cells. Therefore, our prediction was that, in CobB-expressing cells, this increase in the H4K5acyl/acetyl ratio

(B) Total extracts from wild-type and *FASTKD1* KO cells were used to detect the indicated H4K5 and H4K8 modifications as well as actin using the corresponding specific antibodies as indicated. Antibody specificities were confirmed by dot blot analyses on peptides bearing the target H4K5 acylations as well as unrelated acylations (Data S2).
(C) Wild-type and *FASTKD1* KO cells were treated with rotenone (0.5 μM) for 1 or 2 h. Protein extracts were prepared, and the corresponding immunoblots were probed as in (B).
(D) Wild-type and *FASTKD1* KO cells were treated with triascin (3 μM) for 16 h, and protein extracts were prepared and analyzed as in (B).
(E) Wild-type and *FASTKD1* KO cells were treated with ND-630 (100 nM) for 6 h, and extracts were prepared and analyzed as in (B).
(F) Wild-type REH cells were treated with the indicated concentrations of octanoate for 24 h, and the indicated histone PTMs were analyzed as in (B).
(G) Wild-type and *FASTKD1* KO cells were treated with ranolazine (0.5 mM) for 6 h, and protein extracts were analyzed as in (B).
(H) The scheme represents the metabolic pathways targeted by the indicated inhibitors in this series of experiments (D–G). FAO, fatty acid oxidation.
See Figure S3 for accumulation of H4K5 acetylation and various acylations in *FASTKD1* wild-type and KO cells after octanoate treatment. See Tables S1–S3 for details on the unbiased determination of histone H3 and H4 propionylation and butyrylation.

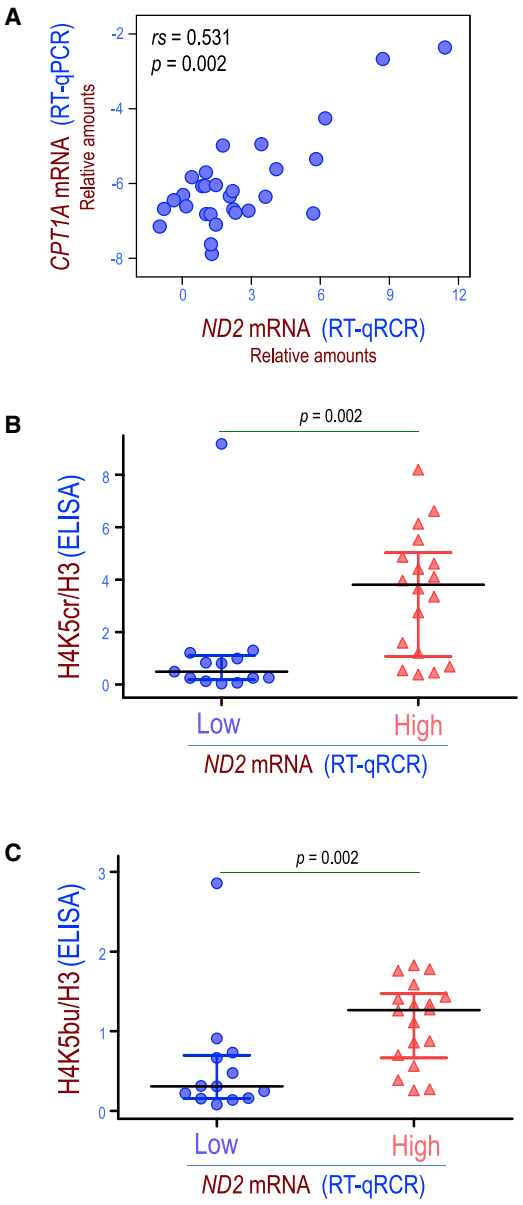

Figure 3. β-Oxidation and mitochondrial activity correlate with histone acylations in B-ALL tumor cells

(A) Total RNAs and proteins were extracted from primary cells from 31 adults with B-ALL, and the relative levels of carnitine palmitate transferase 1A (*CPT1A*), *ND3*, and glyceraldehyde 3-phosphate dehydrogenase (*GAPDH*) mRNAs were measured by qRT-PCR and plotted as shown.

(B and C) In the same samples, the relative amounts of H4K5cr, H4K5bu, and H3 were measured by ELISA. ALL samples were divided into two groups as a function of normalized *ND2* expression, low (blue) and high (red), based on the ROC curve of the qRT-PCR values, as described in the text. In each group, the normalized ELISA values of the H4K5cr/H3 ratio (B) and H4K5bu/H3 ratio (C) are plotted. For each group, the median value (black line) and interquartile range (colored horizontal lines) are shown. Statistical significance of histone acylations between *ND2*-high and -low groups was analyzed with Mann-Whitney *U* test.

See Table S4 for the characteristics of samples from individuals with B-ALL.

should be associated with an increased dynamic of the BRD4-chromatin interaction. We also performed the salt extraction assay described above in control and CobB-expressing COS-7 cells and observed that, similar to REH cells, an increase in the H4K5acyl/acetyl ratio enhances salt elution of BRD4 from chromatin (Figure S4B).

Finally, FRAP was used to precisely measure the dynamics of GFP-BRD4-NUT chromatin interactions in these cells. Figure 4E shows that ectopic expression of CobB and an increased H4K5acylation/acetylation ratio clearly increase the dynamics of BRD4-chromatin interaction.

A metabolically driven increase in H4K5 acylations occurs preferentially on highly acetylated chromatin regions

The distribution of the H4K5cr-bu/H4K5ac ratio was investigated at high resolution in a genome-wide manner. H4K5cr, H4K5bu, and H4K5ac chromatin immunoprecipitation (ChIP) mapping allowed us to visualize the relationship between H4K5cr and H4K5bu with H4K5ac in each of the considered cell lines. The ChIP sequencing (ChIP-seq) read counts corresponding to H4K5cr and H4K5bu were plotted as a function of the read counts corresponding to H4K5ac on gene TSSs. This representation shows a linear correlation between H4K5cr-bu and H4K5ac on TSSs associated with relatively low levels of H4K5ac. However, at higher levels of H4K5ac, this linear relationship is distorted with an increasing H4K5cr-bu/H4K5ac ratio, and this part of the correlation plot best fits a non-linear (exponential regression) model (Figure 5A).

The H4K5cr-bu/H4K5ac ratio controls BRD4 genomic distribution

Anti-BRD4 ChIP-seq experiments were performed to evaluate the effect of the change in H4K5cr-bu/ac ratio on binding of BRD4 to chromatin at high resolution. Focusing on gene TSS regions, we found that BRD4 accumulates on the TSS of highly active genes.

By comparing the levels of TSS region-bound BRD4 between wild-type and *FASTKD1* KO cells, we observed significantly higher levels of BRD4 on the highly active TSSs in the two KO cell lines (see Figures 5B and 5C, showing heatmap and metagene profiles for all genes; see also Figure S5A, showing heatmaps and profiles for a selection of genes with the highest BRD4 peaks in two different anti-BRD4 ChIP-seq experiments). Because there was no change in the total level of BRD4 (Figure 4B, input, and 4C) or in its ability to bind the acetylated H4 tail (Figure 4B, pull-down) in our *FASTKD1* KO cells compared with wild-type cells, we concluded that the observed increase in BRD4 on active gene TSSs in *FASTKD1* KO cells should be due to redistribution of BRD4. Therefore, the increased BRD4 binding to the TSS of highly active genes is very likely a consequence of the genome-wide increase in BRD4 mobility, making BRD4 more available for binding active-gene TSS regions.

Functional significance of the genomic redistribution of BRD4 in REH cells and in ALL malignancies

We reasoned that genes that show a change in expression in *FASTKD1* KO cells compared with wild-type cells should, to

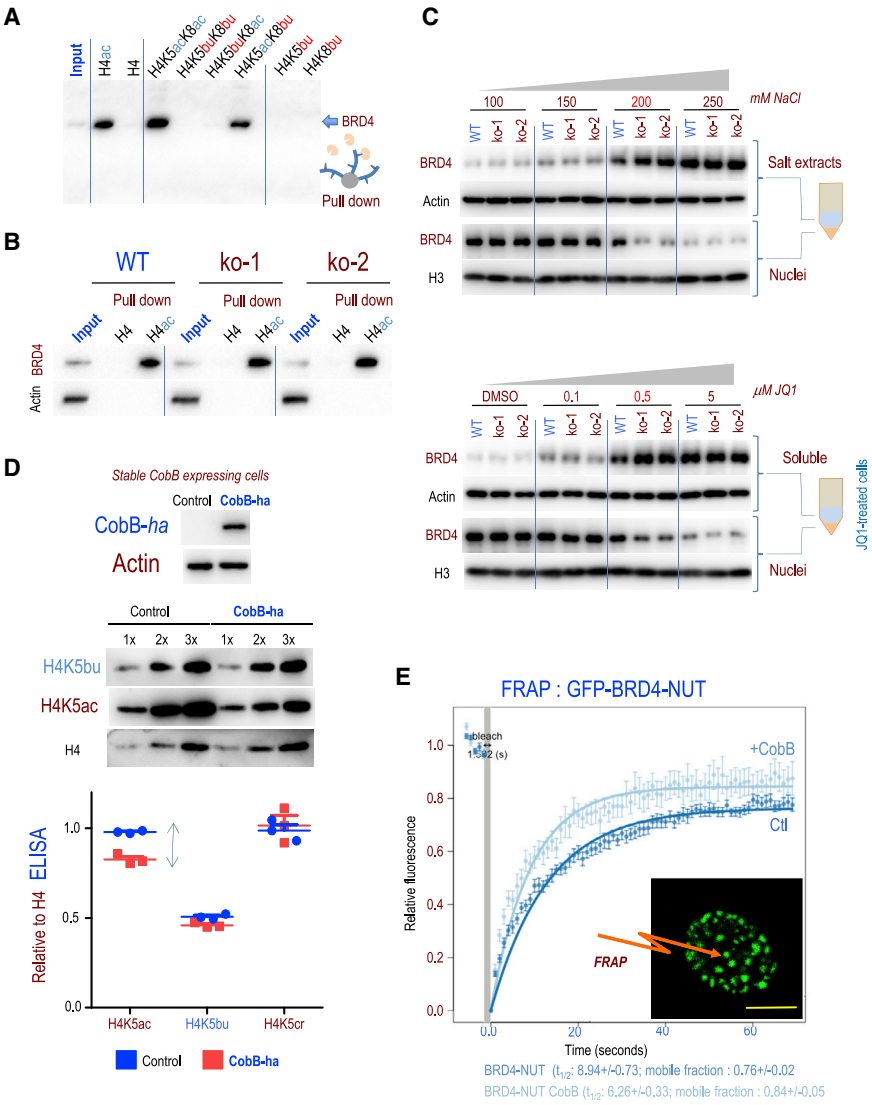

Figure 4. The H4K5 acyl/acetyl ratio controls the dynamics of BRD4-chromatin interaction

(A) Total wild-type REH cell extracts were used in pull-down experiments with the indicated peptides. After pull-down, the peptide-bound proteins were recovered in SDS-PAGE loading buffer and submitted to PAGE, and BRD4 was visualized.

(B) High-salt extracts (total BRD4) from wild-type and *FASTKD1* KO cells were prepared, and a peptide pull-down experiment was performed using unmodified H4 tail peptide or the corresponding acetylated peptide.

(C) Wild-type and *FASTKD1* KO cells were lysed in a buffer containing the indicated concentrations of NaCl. After centrifugation, the corresponding supernatants and pellets (salt extracts and nuclei, respectively) were analyzed by immunoblotting for the presence of BRD4. Actin was also visualized as a loading control for the soluble extracts and H3 for the nucleic fraction (top panels). Wild-type and *FASTKD1* KO cells were treated with the indicated concentrations of JQ1 for 3 h, and cells were lysed and the nuclei pelleted. The soluble extracts and the nucleic fractions were analyzed as above (bottom panels).

(D) Protein extracts were prepared from COS-7 cells stably expressing the hemagglutinin (HA)-tagged bacterial deacetylase *CobB* or from control cells and used to visualize CobB-HA and actin (top panel) or H4 and its indicated modified forms using cell extracts (center panel). 1× to 3× indicate 1-fold to 3-fold loading. The relative amounts of H4, H4K5ac, H4K5bu, and H4K5cr were measured by ELISA in COS-7 cells or in cells expressing CobB-HA in biological triplicates, and the values are presented in the bottom panel (see also Figure S4).

(E) COS-7 cells described in (D), expressing *CobB-HA* or not, were transfected with a GFP-BRD4-NUT expression vector. For each condition, 8 GFP-BRD4-NUT foci (one in each of 8 different cells) were bleached, and the recovery of GFP fluorescence (FRAP) was monitored as a function of time. The datasets corresponding to each FRAP experiment were individually fitted, allowing determination of the half-life (t1/2) of fluorescence recovery and the mobile fractions (values indicated below). The mean ± 2 SEM are shown for each time point. The scale bar represents 10 μm.

See Figure S4A for the selective action of CobB on H4K5 acetylation compared with butyrylation and crotonylation in COS-7 cells. See Figure S4B for the effect of CobB expression in COS-7 cells on BRD4-chromatin interaction stability.

some extent, also be sensitive to the BET bromodomain inhibitor JQ1. To test this hypothesis, we performed RNA-seq on wild-type REH cells treated with different doses of JQ1 and compared the differentially regulated genes (JQ1-responsive genes) with genes that are differentially expressed between wild-type and *FASTKD1* KO REH cells. Interestingly, a significant number of genes differentially expressed in *FASTKD1* KO cells compared with wild-type cells are found among the JQ1-responsive genes (Figures 6A and 6B). Indeed, a subset of genes that are downregulated in FASTKD1 KO REH cells are also downregulated in wild-type REH cells treated with JQ1 (Figure 6B, top panel). Additionally, a significant subset of genes among those that are upregulated in *FASTKD1* KO cells is also downregulated in wild-type JQ1-treated cells (Figure 6B, bottom panel).

The observation that *FASTKD1* KO down- and up- regulated genes are significantly enriched among JQ1-sensitive genes suggests that up- and down- regulated genes have a BRD4-dependent expression.

This is also illustrated by Figure S5, which shows that genes associated with BRD4 peaks are JQ1 sensitive. Indeed, to demonstrate the relationship between redistribution of BRD4 between wild-type and *FASTKD1* KO cells, genes whose TSS regions were associated with high BRD4 peaks and increasing BRD4 binding in KO cells were selected (Figure S5A). This group of genes was used as a gene set for a gene set enrichment analysis (GSEA) analysis to test for its enrichment/depletion in the transcriptomes of JQ1-treated REH cells. Figure S5B shows significant depletion of this

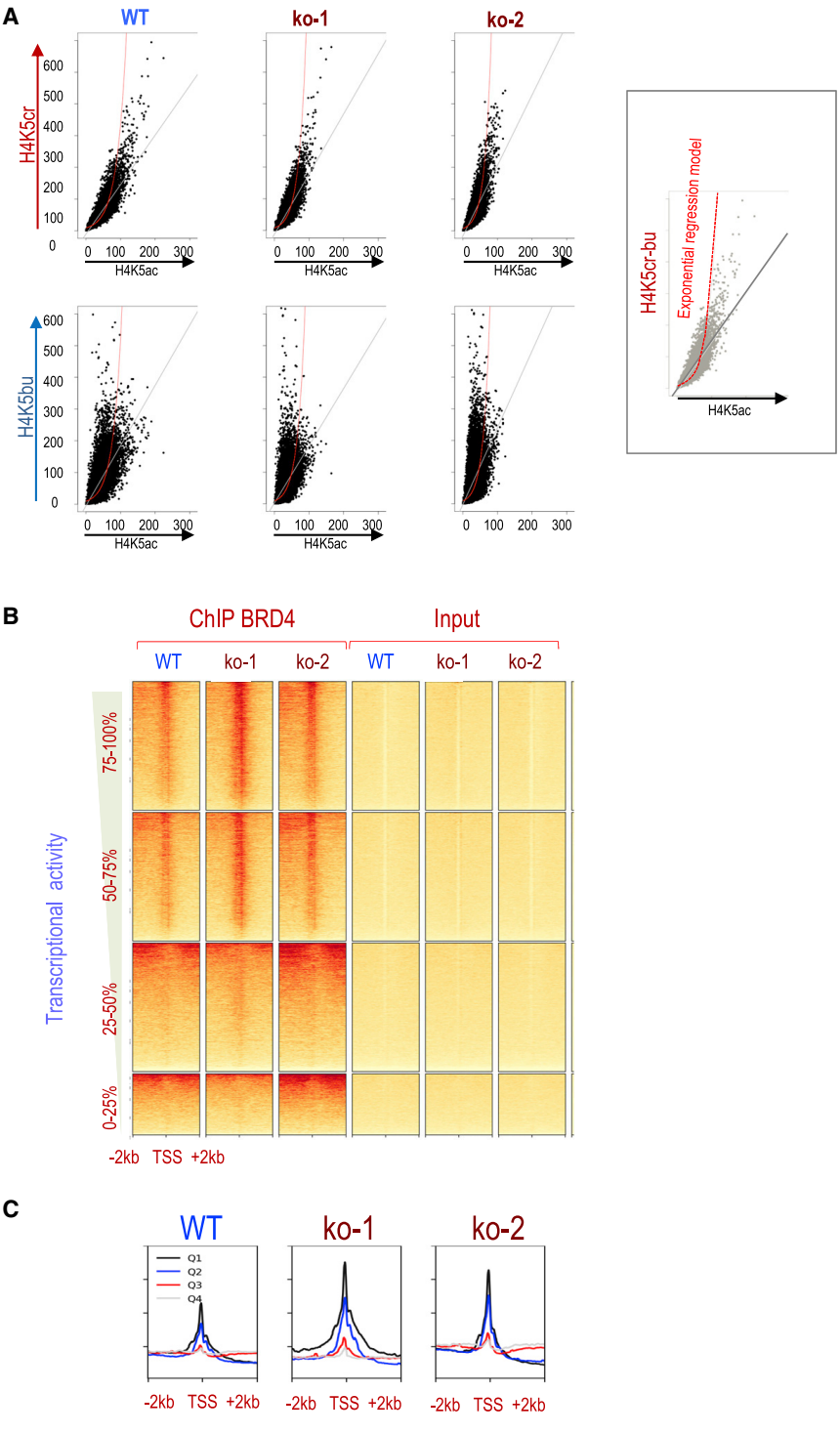

Figure 5. Characterization of the H4K5cr-bu/H4K5ac ratio and BDR4 redistribution between wild-type and *FASTKD1* KO cells

(A) Chromatin from wild-type and *FASTKD1* KO REH cells was extensively digested by micrococcal nuclease (MNase), and the resulting nucleosomes were immunoprecipitated with anti-H4K5ac, anti-H4K5cr, and anti-H4K5bu antibodies and sequenced. The reads were aligned, and the reads per kilobase per million mapped reads (RPKM)-normalized read count values were converted into a 10-bp bin matrix of the signal 2 kb upstream and downstream TSS regions (TSS ± 2,000 bp) using deepTools2 as described in STAR Methods. For all TSSs, the mean normalized read counts/TSS were calculated for each genotype (wild-type, KO-1, and KO-2) and each experiment H4K5cr, H4K5bu, and H4K5ac. Considering each genotype, the TSS regions were then plotted according to their mean normalized read counts for H4K5cr (top panels) or H4K5bu (bottom panels) ChIP-seq (y axis) as a function of their mean normalized read counts for H4K5ac ChIP-seq (x axis). To evaluate the relationship between the measured parameters, non-acetyl acylations and acetylation of H4 lysine 5 (H4K5ac), in wild-type cells and in the two FASTKD1 KO cells, a linear regression model (gray lines) and an exponential regression model (red lines) were fitted.

(B and C) Anti-BRD4 ChIP-seqs were performed on MNase-digested chromatin of wild-type and *FASTKD1* KO cell lines. The heatmap (B) and profiles (C) show BRD4 ChIP-seq normalized read counts in wild-type as well as in *FASTKD1* KO REH cells over all gene TSS-centered regions (TSSs ± 2,000 bp). The TSSs were ranked as a function of their transcriptional activity in wild-type REH cells and grouped into quartiles (Q1, Q2, Q3, and Q4), with Q1 (75%–100%) corresponding to the 25% of genes with highest expression and Q4 to the lowest 25% (0%–25%). These gene groups are shown on the heatmap from top to bottom: highest (Q1, 75%–100%) to lowest (Q4, 0%–25%) gene expression levels (B). The profiles corresponding to the different quartile groups are shown in different colors as indicated (C).

See Figure S5, showing that genes with increased BRD4 peaks in *FASTKD1* KO cells are JQ1 sensitive.

group of genes, illustrating their downregulation in JQ1-treated cells, which demonstrates that their expression is BRD4 dependent.

To show that this H4K5 acylation- and BRD4- dependent regulatory circuit could also be involved in B-ALL tumor cells, we analyzed the transcriptomes of a subset of B-ALL tumors (Table S4) for which we had measurements of H4K5bu and H4K5cr levels (Figure 3).

We performed RNA-seq on 25 B-ALL samples and identified genes differentially expressed between the two groups of H4K5cr-bu-high (n = 15) and H4K5cr-bu-low (n = 10) B-ALL (Figure S6). We then compared the list of differentially expressed genes between these two categories of ALL cells (Figure 6C) with the list of differentially expressed genes between REH wild-type and *FASTKD1* KO REH cells (Figure 6A), which also showed higher levels of H4K5cr-bu compared with wild-type

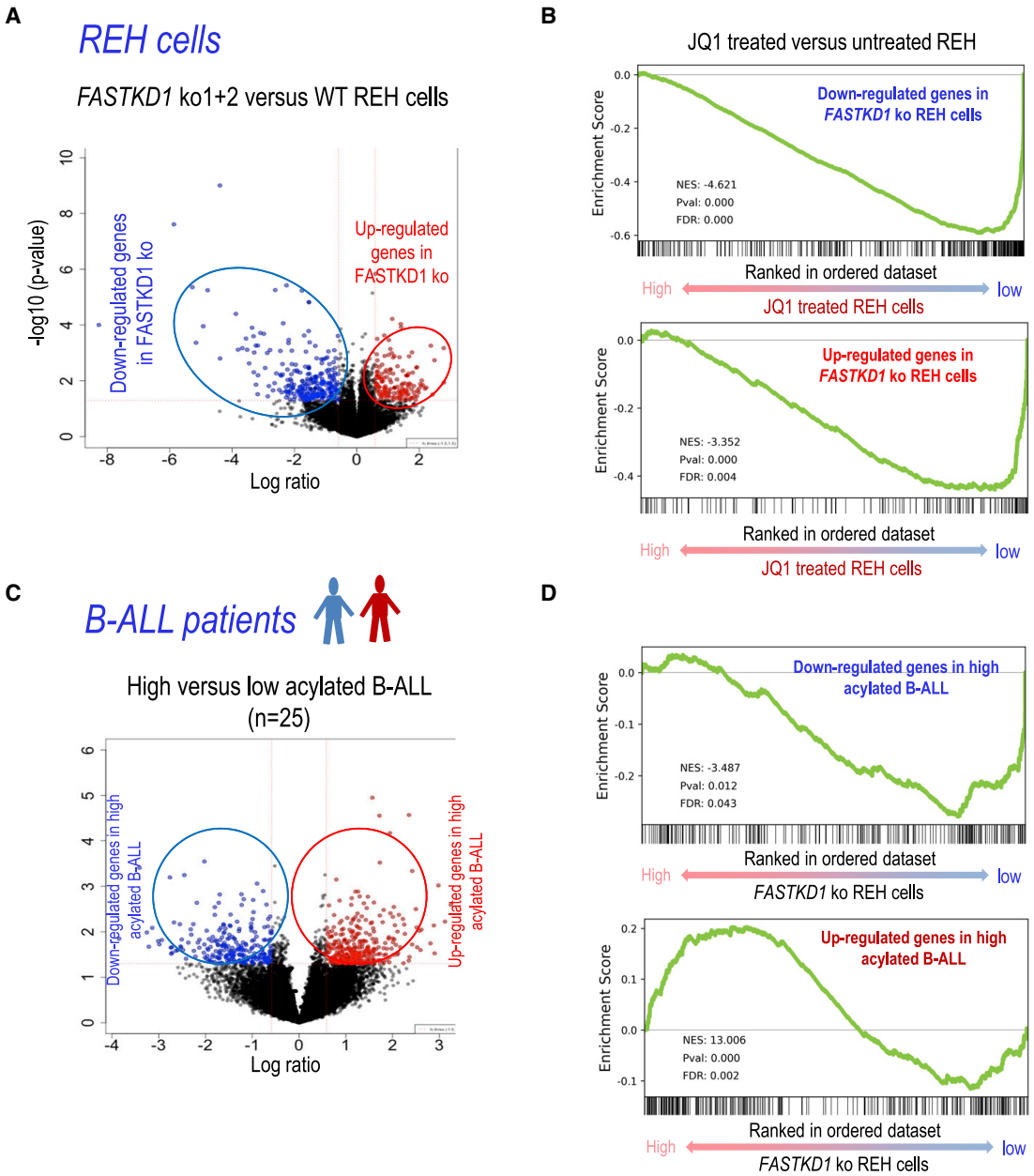

Figure 6. Mitochondrial activity drives H4K5 acylations and directs BRD4-dependent gene expression in the REH cell line and in blasts from individuals with B-ALL

(A) Volcano plot illustrating the differential gene expression signature between *FASTKD1* KO (KO-1 and KO-2) and wild-type REH cells. y axis: −log10 (p value); x axis: log (ratio of normalized expression values between *KO* and wild-type cells). The genes downregulated or upregulated with a fold change greater than 1.5 and a Student's t test p value of less than 0.05 are represented in blue and red, respectively.

(B) The two gene groups defined in (A) were used as gene sets for GSEA plots to test for their enrichment/depletion in JQ1-treated REH cells. These plots show significant depletion of genes up- or downregulated in *FASTKD1* KO cells. Both of these gene categories are therefore JQ1 sensitive.

(C) Volcano plot illustrating the differential gene expression signature between B-ALL blasts with high H4K5 acylations (crotonylation and/or butyrylation, n = 15) and B-ALL blasts with low acylations (n = 10). y axis: −log10 (p value); x axis: log (ratio of normalized expression values between B-ALL with high and low acylation levels). Genes downregulated or upregulated with an absolute fold change greater than 1.5 and a Student's t test p value of less than 0.05 are represented in blue and red, respectively.

(D) The two gene groups defined in (C) were used as gene sets for GSEA plots to test their enrichment/depletion in the *FASTKD1* KO REH cells. These plots show significant depletion or enrichment of genes down- or upregulated, respectively, in *FASTKD1* KO cells, suggesting that the transcriptional effect of high acylation in B-ALL blasts is similar to the effect of *FASTKD1* KO-induced high acylation in REH cells.

See Figure S6, showing differential expression between B-ALL blasts with high compared with low acylation levels. See Figure S7 for the GSEA of the transcriptomic signatures of REH cells (*FASTKD1* KO versus the wild type or JQ1-treated versus untreated) and B-ALL with high versus low H4K5cr/bu levels.

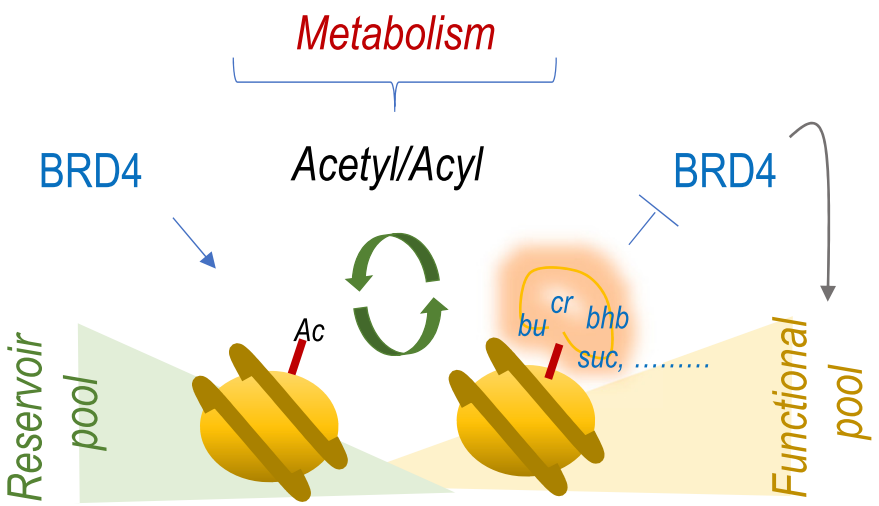

Figure 7. Control of the BRD4 reservoir by mitochondrial activity and cell metabolism: A working model

Enhanced mitochondrial activity leads to a global increase in the histone H4K5 acylation/acetylation ratio. Bromodomain-containing factors, such as BRD4, lose their tight binding to the genome-wide acetylated nucleosomes (reservoir pool) and therefore become available to be redistributed from this reservoir pool toward specific and localized genome regions, including active genes' TSSs (functional pool).

cells (Figure 2). Interestingly, the two transcriptional signatures share similarities because a significant number of genes are regulated in the same manner in *FASTKD1* KO REH and H4K5cr-bu-high B-ALL cells (Figure 6D). It is noteworthy that the common point between these two systems is the comparison between the state of H4K5 acylations.

Accordingly, the GSEA shows that, in REH *FASTKD1* KO cells and H4K5cr-bu-high B-ALL cells from affected individuals, genes encoding for mitochondrial functions are significantly upregulated, confirming the presence of active mitochondria in these cells (Figure S7, top panels). Other common features are shared by the expression signatures of both of these cells, including high translational and proliferation/cell cycle-related activities and significant depletion in hematopoietic stem cells genes (Figure S7).

DISCUSSION

Fatty acid β-oxidation has been shown to be a major source of acetyl-CoA driving histone acetylation (McDonnell et al., 2016). Our present investigations reveal that mitochondrial activity, and fatty acid β-oxidation in particular, are also the main source of histone acylations. Interestingly, this conclusion is in full agreement with the recent finding identifying fatty acid β-oxidation, which, in yeast, takes place in peroxisomes, as a driver of histone crotonylation in *S. cerevisiae*, particularly during yeast metabolic cycles (Gowans et al., 2019).

As demonstrated here, histone acylations occur preferentially and, hence, concentrate on regions with high levels of histone acetylations. The functional meaning of this observation is that the sum of a series of low-abundance histone acylations and their local concentration on specific regions could make a significant contribution to non-acetyl histone modifications, in terms of stoichiometry and gene expression regulation, by competing with histone acetylation. This situation should have a direct effect on the stability of the interaction between bromodomains and chromatin. Indeed, structural studies have demonstrated why most of the bromodomains are unable to bind longer acyllysine modifications and how these modifications could attract other types of binder factors (Andrews et al., 2016b). Consequently, an increase in histone acylations/acetylation ratio, although destabilizing chromatin binding by bromodomains, could, in contrast, stabilize the interaction of factors bearing YEATS and DPF domains, which could, in turn, enhance displacement of bromodomain factors and their increased mobility.

Another important concept developed here is that of a bromodomain factor "reservoir." The pool of BRD4 bound to the genome-wide bulk of acetylated nucleosomes could be considered a reservoir of BRD4. As shown here, a general increase of more than 3C acylations on H4K5 leads to a global increase in the solubility of BRD4. This "mobile" fraction of BRD4 would be released from numerous genomic sites and concentrate on a limited number of "hyperdynamic" chromatin loci, such as active-gene TSSs. This explains the increase in BRD4 binding observed upon *FASTKD1* inactivation at highly active gene TSSs in our ChIP-seq mappings. This mechanism should also make BRD4 available for interactions with the TSS-bound non-histone proteins, including the acetylated cyclin T1 subunit of positive transcription elongating factor B (p-TEFb), in a bromodomain-dependent (Schröder et al., 2012) and independent (Lambert et al., 2019) manner.

We also took advantage of quantitative measurements of H4K5bu and H4K5cr in B-ALL samples to investigate the relationship between gene expression and the level of H4K5 acylations. The correlation between the level of expression of the mitochondrial gene *ND2* and the level of H4K5bu-cr in samples from these individuals suggests that our observation made in REH cells can be extended to affected individuals' B-ALL blast cells, where high mitochondrial transcriptional activity is also associated with an increased H4K5 acylation/acetylation ratio.

Based on all of these data, we propose that activation of mitochondrial activity leads to an increase in H4K5 acylation (butyrylation, crotonylation, etc.), loosening the binding of the genome-wide bulk of acetylated nucleosomes by BRD4 (BRD4 reservoir), making it available for recruitment and binding at active-gene regulatory sites (Figure 7). In the frame of ALL, we also propose that a decrease of mitochondrial activity in blasts because of aberrant *FASTKD1* expression or for any other reasons, could favor a gene expression pattern associated with aggressive forms of this pathology (Wang et al., 2015).

Overall, this work highlights several important concepts in the biology of chromatin and transcription. We propose that there is systematic co-existence of histone acetylation and histone acylations at chromatin dynamic spots. With respect to the function of bromodomain factors, histone acylations should be considered collectively and not individually. In terms of stoichiometry relative to acetylation, more than 3C histone acylations, including butyrylation, crotonylation, etc., are permanently exchanged and, hence, should be considered one functional entity. Histone acylations occur and concentrate on regions of high histone acetylation. The ratio of histone acyl/acetyl is a critical functional parameter tuned by upstream cell metabolic reactions. Mitochondrial activity and β-oxidation in particular are important drivers of histone acylations. The histone acyl/acetyl ratio fine-tunes the availability of BRD4 for recruitment at its sites of action and could represent a general means of controlling bromodomain-containing factor availability and function.

STAR★METHODS

Detailed methods are provided in the online version of this paper and include the following:

- KEY RESOURCES TABLE
- RESOURCE AVAILABILITY
  - Lead contact
  - Materials availability
  - Data and code availability
- EXPERIMENTAL MODEL AND SUBJECT DETAILS
  - Cell lines and cell cultures
  - CRISPR/Cas9 mediated knockout cell line
  - B-ALL patients' bone marrow samples
- METHOD DETAILS
  - Drug treatment and sample preparations
  - Plasmids, shRNA and sgRNA
  - Lentivirus production and infection
  - Histone preparation
  - MS quantification of histone acylations
  - Peptide pull-down assay
  - Western blotting
  - Relative quantification of histone acylations with ELISA
  - Immunofluorescence
  - Fluorescence recovery after photobleaching (FRAP)
  - Metabolic assay
  - RT-qPCR
  - RNA-seq
  - ChIP-seq
- QUANTIFICATION AND STATISTICAL ANALYSIS

SUPPLEMENTAL INFORMATION

Supplemental information can be found online at https://doi.org/10.1016/j.celrep.2021.109460.

ACKNOWLEDGMENTS

This program was supported by Fondation ARC program RF20190208471, the ANR Episperm4 program, the "Université Grenoble Alpes" ANR-15-IDEX-02 LIFE and SYMER programs, INCa and IreSP, Plan Cancer Pitcher, MSD Avenir ERICAN programs, as well as the Cancer ITMO (Multi-Organisation Thematic Institute) of the French Alliance for Life Sciences and Health (AVIESAN) MIC program. J.M.'s lab is supported by the National Natural Science Foundation of China (81670147), the clinical research plan of the Shanghai Hospital Development Center (16CR3008A), international cooperation projects of the Shanghai Science and Technology Committee (15410710200), and the innovation program of the Shanghai Municipal Education Commission (8201001096). M.G. follows a Shanghai Jiao Tong University-Grenoble Alpes University joint PhD program of Cai Yuanpei-Campus de France supported by the China Scholarship Council. This work was supported by the University of Chicago, the Nancy and Leonard Florsheim Family Fund (to Y.Z.), and NIH grants GM135504 and DK118266 (to Y.Z.). M.T.'s group acknowledges funding from the Natural Science Foundation of China (91753203). The TGML Platform is supported by grants from Inserm, GIS IBiSA, Aix-Marseille Université, and ANR-10-INBS-0009-10. N.H. and S.M.'s work was funded by the Max Planck Institute of Molecular Physiology.

AUTHOR CONTRIBUTIONS

M.G. generated model cell lines and performed most of the experiments. M.T. performed H3 and H4 PTM measurements. L.B. prepared all libraries and performed sequencing under the supervision of D.P. S.R. performed and supervised all bioinformatics analyses, also involving F.C. and E.B.-F. M.S. and H.N. produced the CobB expression vector and discussed the results. S.C. performed the FRAP experiments and analyzed the data with help from F.C. S.B. performed anti-H4K5ac-cr ChIP experiments, and T.W., S.W., and W.X. helped with the qRT-PCR experiments. Z.C. produced and characterized the anti-histone PTM antibodies. J.L. helped with and discussed the statistical analyses. J.W. recruited the individuals with B-ALL and took care of the biobank setup and formalities, including acquisition of ethics committee approval. L.P., J.R., and Y.L. helped with collection and disposition of samples from affected individuals. J.-Q.M. supervised the clinical part of the experiments and co-supervised M.G.'s work. Y.Z. supervised the work on histone PTMs, provided access to antibodies, and helped with data interpretation. S.K. designed and coordinated the whole project and wrote the manuscript. All authors read and commented on the manuscript.

DECLARATION OF INTERESTS

Y.Z. is a founder, board member, advisor to, and inventor on patents licensed to PTM Biolabs Inc. (Hangzhou, China and Chicago, IL) and Maponos Therapeutics Inc. (Chicago, IL). Z.C. is an employee and equity holder of PTM BioLabs Inc.

Received: January 4, 2021
Revised: May 11, 2021
Accepted: July 8, 2021
Published: July 27, 2021

SUPPORTING CITATIONS

The following reference appears in the Supplemental information: Popow et al. (2015).

REFERENCES

Anders, S., Pyl, P.T., and Huber, W. (2015). HTSeq–a Python framework to work with high-throughput sequencing data. Bioinformatics *31*, 166–169.

Andrews, F.H., Shinsky, S.A., Shanle, E.K., Bridgers, J.B., Gest, A., Tsun, I.K., Krajewski, K., Shi, X., Strahl, B.D., and Kutateladze, T.G. (2016a). The Taf14 YEATS domain is a reader of histone crotonylation. Nat. Chem. Biol. *12*, 396–398.

Andrews, F.H., Strahl, B.D., and Kutateladze, T.G. (2016b). Insights into newly discovered marks and readers of epigenetic information. Nat. Chem. Biol. *12*, 662–668.

Bao, X., Liu, Z., Zhang, W., Gladysz, K., Fung, Y.M.E., Tian, G., Xiong, Y., Wong, J.W.H., Yuen, K.W.Y., and Li, X.D. (2019). Glutarylation of Histone H4 Lysine 91 Regulates Chromatin Dynamics. Mol. Cell *76*, 660–675.e9.

Barral, S., Morozumi, Y., Tanaka, H., Montellier, E., Govin, J., de Dieuleveult, M., Charbonnier, G., Couté, Y., Puthier, D., Buchou, T., et al. (2017). Histone Variant H2A.L.2 Guides Transition Protein-Dependent Protamine Assembly in Male Germ Cells. Mol. Cell *66*, 89–101.e8.

Buchou, T., Tan, M., Barral, S., Vitte, A.L., Rousseaux, S., Arechaga, J., and Khochbin, S. (2017). Purification and Analysis of Male Germ Cells from Adult Mouse Testis. Methods Mol. Biol. *1510*, 159–168.

Chen, Y., Sprung, R., Tang, Y., Ball, H., Sangras, B., Kim, S.C., Falck, J.R., Peng, J., Gu, W., and Zhao, Y. (2007). Lysine propionylation and butyrylation are novel post-translational modifications in histones. Mol. Cell. Proteomics *6*, 812–819.

Crespo, M., Damont, A., Blanco, M., Lastrucci, E., Kennani, S.E., Ialy-Radio, C., Khattabi, L.E., Terrier, S., Louwagie, M., Kieffer-Jaquinod, S., et al. (2020). Multi-omic analysis of gametogenesis reveals a novel signature at the promoters and distal enhancers of active genes. Nucleic Acids Res. *48*, 4115–4138.

Dai, B., Dahmani, F., Cichocki, J.A., Swanson, L.C., and Rasmussen, T.P. (2011). Detection of post-translational modifications on native intact nucleosomes by ELISA. J. Vis. Exp., 2593.

Dai, L., Peng, C., Montellier, E., Lu, Z., Chen, Y., Ishii, H., Debernardi, A., Buchou, T., Rousseaux, S., Jin, F., et al. (2014). Lysine 2-hydroxyisobutyrylation is a widely distributed active histone mark. Nat. Chem. Biol. *10*, 365–370.

Dobin, A., Davis, C.A., Schlesinger, F., Drenkow, J., Zaleski, C., Jha, S., Batut, P., Chaisson, M., and Gingeras, T.R. (2013). STAR: ultrafast universal RNA-seq aligner. Bioinformatics *29*, 15–21.

Dull, T., Zufferey, R., Kelly, M., Mandel, R.J., Nguyen, M., Trono, D., and Naldini, L. (1998). A third-generation lentivirus vector with a conditional packaging system. J. Virol. *72*, 8463–8471.

Emadali, A., Rousseaux, S., Bruder-Costa, J., Rome, C., Duley, S., Hamaidia, S., Betton, P., Debernardi, A., Leroux, D., Bernay, B., et al. (2013). Identification of a novel BET bromodomain inhibitor-sensitive, gene regulatory circuit that controls Rituximab response and tumour growth in aggressive lymphoid cancers. EMBO Mol. Med. *5*, 1180–1195.

Flynn, E.M., Huang, O.W., Poy, F., Oppikofer, M., Bellon, S.F., Tang, Y., and Cochran, A.G. (2015). A Subset of Human Bromodomains Recognizes Butyryllysine and Crotonyllysine Histone Peptide Modifications. Structure *23*, 1801–1814.

Fujisawa, T., and Filippakopoulos, P. (2017). Functions of bromodomain-containing proteins and their roles in homeostasis and cancer. Nat. Rev. Mol. Cell Biol. *18*, 246–262.

Goudarzi, A., Zhang, D., Huang, H., Barral, S., Kwon, O.K., Qi, S., Tang, Z., Buchou, T., Vitte, A.L., He, T., et al. (2016). Dynamic Competing Histone H4 K5K8 Acetylation and Butyrylation Are Hallmarks of Highly Active Gene Promoters. Mol. Cell *62*, 169–180.

Gowans, G.J., Bridgers, J.B., Zhang, J., Dronamraju, R., Burnetti, A., King, D.A., Thiengmany, A.V., Shinsky, S.A., Bhanu, N.V., Garcia, B.A., et al. (2019). Recognition of Histone Crotonylation by Taf14 Links Metabolic State to Gene Expression. Mol. Cell *76*, 909–921.e3.

Haws, S.A., Leech, C.M., and Denu, J.M. (2020). Metabolism and the Epigenome: A Dynamic Relationship. Trends Biochem. Sci. *45*, 731–747.

Huang, H., Zhang, D., Wang, Y., Perez-Neut, M., Han, Z., Zheng, Y.G., Hao, Q., and Zhao, Y. (2018). Lysine benzoylation is a histone mark regulated by SIRT2. Nat. Commun. *9*, 3374.

Jin, H., Kasper, L.H., Larson, J.D., Wu, G., Baker, S.J., Zhang, J., and Fan, Y. (2020). ChIPseqSpikeInFree: a ChIP-seq normalization approach to reveal global changes in histone modifications without spike-in. Bioinformatics *36*, 1270–1272.

Jourdain, A.A., Popow, J., de la Fuente, M.A., Martinou, J.C., Anderson, P., and Simarro, M. (2017). The FASTK family of proteins: emerging regulators of mitochondrial RNA biology. Nucleic Acids Res. *45*, 10941–10947.

Kebede, A.F., Nieborak, A., Shahidian, L.Z., Le Gras, S., Richter, F., Gómez, D.A., Baltissen, M.P., Meszaros, G., Magliarelli, H.F., Taudt, A., et al. (2017). Histone propionylation is a mark of active chromatin. Nat. Struct. Mol. Biol. *24*, 1048–1056.

Lambert, J.P., Picaud, S., Fujisawa, T., Hou, H., Savitsky, P., Uusküla-Reimand, L., Gupta, G.D., Abdouni, H., Lin, Z.Y., Tucholska, M., et al. (2019). Interactome Rewiring Following Pharmacological Targeting of BET Bromodomains. Mol. Cell *73*, 621–638.e17.

Langmead, B., and Salzberg, S.L. (2012). Fast gapped-read alignment with Bowtie 2. Nat. Methods *9*, 357–359.

Li, Y., Sabari, B.R., Panchenko, T., Wen, H., Zhao, D., Guan, H., Wan, L., Huang, H., Tang, Z., Zhao, Y., et al. (2016). Molecular Coupling of Histone Crotonylation and Active Transcription by AF9 YEATS Domain. Mol. Cell *62*, 181–193.

Lozoya, O.A., Wang, T., Grenet, D., Wolfgang, T.C., Sobhany, M., Ganini da Silva, D., Riadi, G., Chandel, N., Woychik, R.P., and Santos, J.H. (2019). Mitochondrial acetyl-CoA reversibly regulates locus-specific histone acetylation and gene expression. Life Sci. Alliance *2*, e201800228.

Matilainen, O., Quirós, P.M., and Auwerx, J. (2017). Mitochondria and Epigenetics - Crosstalk in Homeostasis and Stress. Trends Cell Biol. *27*, 453–463.

McDonnell, E., Crown, S.B., Fox, D.B., Kitir, B., Ilkayeva, O.R., Olsen, C.A., Grimsrud, P.A., and Hirschey, M.D. (2016). Lipids Reprogram Metabolism to Become a Major Carbon Source for Histone Acetylation. Cell Rep. *17*, 1463–1472.

Olp, M.D., Zhu, N., and Smith, B.C. (2017). Metabolically Derived Lysine Acylations and Neighboring Modifications Tune the Binding of the BET Bromodomains to Histone H4. Biochemistry *56*, 5485–5495.

Popow, J., Alleaume, A.M., Curk, T., Schwarzl, T., Sauer, S., and Hentze, M.W. (2015). FASTKD2 is an RNA-binding protein required for mitochondrial RNA processing and translation. RNA *21*, 1873–1884.

Pougovkina, O., te Brinke, H., Ofman, R., van Cruchten, A.G., Kulik, W., Wanders, R.J., Houten, S.M., and de Boer, V.C. (2014). Mitochondrial protein acetylation is driven by acetyl-CoA from fatty acid oxidation. Hum. Mol. Genet. *23*, 3513–3522.

Ramírez, F., Ryan, D.P., Grüning, B., Bhardwaj, V., Kilpert, F., Richter, A.S., Heyne, S., Dündar, F., and Manke, T. (2016). deepTools2: a next generation web server for deep-sequencing data analysis. Nucleic Acids Res. *44* (*W1*), W160-5.

Reynoird, N., Schwartz, B.E., Delvecchio, M., Sadoul, K., Meyers, D., Mukherjee, C., Caron, C., Kimura, H., Rousseaux, S., Cole, P.A., et al. (2010). Oncogenesis by sequestration of CBP/p300 in transcriptionally inactive hyperacetylated chromatin domains. EMBO J. *29*, 2943–2952.

Sabari, B.R., Tang, Z., Huang, H., Yong-Gonzalez, V., Molina, H., Kong, H.E., Dai, L., Shimada, M., Cross, J.R., Zhao, Y., et al. (2015). Intracellular crotonyl-CoA stimulates transcription through p300-catalyzed histone crotonylation. Mol. Cell *58*, 203–215.

Sanjana, N.E., Shalem, O., and Zhang, F. (2014). Improved vectors and genome-wide libraries for CRISPR screening. Nat. Methods *11*, 783–784.

Schneider, C.A., Rasband, W.S., and Eliceiri, K.W. (2012). NIH Image to ImageJ: 25 years of image analysis. Nat. Methods *9*, 671–675.

Schröder, S., Cho, S., Zeng, L., Zhang, Q., Kaehlcke, K., Mak, L., Lau, J., Bisgrove, D., Schnölzer, M., Verdin, E., et al. (2012). Two-pronged binding with bromodomain-containing protein 4 liberates positive transcription elongation factor b from inactive ribonucleoprotein complexes. J. Biol. Chem. *287*, 1090–1099.

Shiota, H., Barral, S., Buchou, T., Tan, M., Couté, Y., Charbonnier, G., Reynoird, N., Boussouar, F., Gérard, M., Zhu, M., et al. (2018). Nut Directs p300-Dependent, Genome-Wide H4 Hyperacetylation in Male Germ Cells. Cell Rep. *24*, 3477–3487.e6.

Simithy, J., Sidoli, S., Yuan, Z.F., Coradin, M., Bhanu, N.V., Marchione, D.M., Klein, B.J., Bazilevsky, G.A., McCullough, C.E., Magin, R.S., et al. (2017).

Characterization of histone acylations links chromatin modifications with metabolism. Nat. Commun. *8*, 1141.

Smestad, J., Erber, L., Chen, Y., and Maher, L.J., 3rd. (2018). Chromatin Succinylation Correlates with Active Gene Expression and Is Perturbed by Defective TCA Cycle Metabolism. iScience *2*, 63–75.

Spinck, M., Neumann-Staubitz, P., Ecke, M., Gasper, R., and Neumann, H. (2020). Evolved, Selective Erasers of Distinct Lysine Acylations. Angew. Chem. Int. Ed. Engl. *59*, 11142–11149.

Tan, M., Luo, H., Lee, S., Jin, F., Yang, J.S., Montellier, E., Buchou, T., Cheng, Z., Rousseaux, S., Rajagopal, N., et al. (2011). Identification of 67 histone marks and histone lysine crotonylation as a new type of histone modification. Cell *146*, 1016–1028.

Tarazona, O.A., and Pourquié, O. (2020). Exploring the Influence of Cell Metabolism on Cell Fate through Protein Post-translational Modifications. Dev. Cell *54*, 282–292.

Trefely, S., Lovell, C.D., Snyder, N.W., and Wellen, K.E. (2020). Compartmentalised acyl-CoA metabolism and roles in chromatin regulation. Mol. Metab. *38*, 100941.

Wang, J., Mi, J.Q., Debernardi, A., Vitte, A.L., Emadali, A., Meyer, J.A., Charmpi, K., Ycart, B., Callanan, M.B., Carroll, W.L., et al. (2015). A six gene expression signature defines aggressive subtypes and predicts outcome in childhood and adult acute lymphoblastic leukemia. Oncotarget *6*, 16527–16542.

Weber, K., Bartsch, U., Stocking, C., and Fehse, B. (2008). A multicolor panel of novel lentiviral "gene ontology" (LeGO) vectors for functional gene analysis. Mol. Ther. *16*, 698–706.

Xie, Z., Zhang, D., Chung, D., Tang, Z., Huang, H., Dai, L., Qi, S., Li, J., Colak, G., Chen, Y., et al. (2016). Metabolic Regulation of Gene Expression by Histone Lysine β-Hydroxybutyrylation. Mol. Cell *62*, 194–206.

Xiong, X., Panchenko, T., Yang, S., Zhao, S., Yan, P., Zhang, W., Xie, W., Li, Y., Zhao, Y., Allis, C.D., and Li, H. (2016). Selective recognition of histone crotonylation by double PHD fingers of MOZ and DPF2. Nat. Chem. Biol. *12*, 1111–1118.

Zhang, D., Tang, Z., Huang, H., Zhou, G., Cui, C., Weng, Y., Liu, W., Kim, S., Lee, S., Perez-Neut, M., et al. (2019). Metabolic regulation of gene expression by histone lactylation. Nature *574*, 575–580.

STAR★METHODS

KEY RESOURCES TABLE

REAGENT or RESOURCE	SOURCE	IDENTIFIER
Antibodies		
Rabbit monoclonal anti-BRD4 (WB and ChIP)	Bethyl Lab	Cat# A301-985A100; RRID: AB_2620184
Rabbit polyclonal anti-H4K5bu (WB and ELISA)	PTM biolabs	Cat#PTM-313
Rabbit polyclonal anti-H4K5bu (ChIP)	PTM biolabs	Cat#PTM-310
Rabbit polyclonal anti-H4K8bu (WB)	PTM biolabs	Cat#PTM-311
Rabbit polyclonal anti-H4K5cr (WB, ChIP and ELISA)	PTM biolabs	Cat#PTM-521
Rabbit polyclonal anti-H4K8cr (WB)	PTM biolabs	Cat#PTM-522
Rabbit polyclonal anti-H4K5ac (WB)	PTM biolabs	Cat#PTM-119
Rabbit polyclonal anti-H4K8ac (WB)	PTM biolabs	Cat#PTM-120
Rabbit polyclonal anti-H4K5bhb (WB)	PTM biolabs	Cat#PTM-1205
Rabbit polyclonal anti-H4K5lac (WB)	PTM biolabs	Cat#PTM-1407
Rabbit monoclonal anti-H4K5ac (ChIP)	Abcam	Cat#ab51997; RRID: AB_2264109
Rabbit polyclonal anti-HA (WB and ELISA)	Abcam	Cat#ab9110; RRID: AB_307019
Rabbit polyclonal anti-H4 (WB and ELISA)	Abcam	Cat#ab10158; RRID: AB_296888
Mouse monoclonal anti-Flag M2 (IF)	Sigma-Aldrich	Cat#F1804; RRID: AB_262044
Mouse monoclonal Anti-β-Actin (WB)	Sigma-Aldrich	Cat#A5441; RRID: AB_476744
Rabbit polyclonal H3 antibody (ELISA)	Abcam	Cat#ab1791; RRID: AB_302613
Goat anti-Rabbit IgG (H+L)-HRP (WB and ELISA)	Bio-rad	Cat#1706515, RRID: AB_2617112
Goat anti-Mouse IgG (H+L)-HRP (WB)	Bio-rad	Cat#170-6516; RRID: AB_11125547
Goat anti-Rabbit IgG, HRP linked antibody (ELISA)	Cell Signaling Technology	Cat#7074; RRID: AB_2099233
Goat anti-Mouse IgG (H+L), DyLight 405 (IF)	Invitrogen	Cat# 35501BID; RRID: AB_2533209
Bacterial and virus strains		
One shot Stbl3 Competent *E. coli*	Invitrogen	Cat#C737303
Biological samples		
B-ALL patients' bone marrow samples, see Table S4	This paper	N/A
Chemicals, peptides, and recombinant proteins		
JQ-1	Emadali et al., 2013	N/A
Rotenone	Sigma-Aldrich	Cat#R8875
Oligomycin A	Sigma-Aldrich	Cat#75351
Antimycin A	Sigma-Aldrich	Cat#A8674
FCCP	Sigma-Aldrich	Cat#C2920
Sodium octanoate	Sigma-Aldrich	Cat#C5038
Ranolazine	Sigma-Aldrich	Cat#R6152
Triacsin C	Sigma-Aldrich	Cat#T4540
ND-630 (Firsocostat)	MedChemExpress	Cat#HY-16901
Puromycin	Sigma-Aldrich	Cat#P8833
Mitotracker Red	Invitrogen	Cat#M7512
Micrococcal nuclease S7	Sigma-Aldrich	Cat#10107921001
Lipofectamine 2000	Invitrogen	Cat#11668019
Complete Mini protease inhibitors	Sigma-Aldrich	Cat #11836153001

(*Continued on next page*)

Continued

REAGENT or RESOURCE	SOURCE	IDENTIFIER
All histone peptides used in this study (H4 /H4K5acK8ac /H4K5buK8bu /H4K5acK8bu /H4K5buK8ac /H4K5bu /H4K8bu)	Goudarzi et al., 2016	N/A
LymphoPrep Solution	Axis Shield PoC	Cat#1114547
Gelatin solution	Sigma-Aldrich	Cat#G1393
TRIzol reagent	Invitrogen	Cat#15596018
Trichostatin A (TSA)	Sigma-Aldrich	Cat#T8852
Trichloroacetic Acid (TCA)	Sigma-Aldrich	Cat#T-0699
n-Butryric acid	Sigma-Aldrich	Cat#B-2503
Dynabeads protein G	Thermo Fisher	Cat#10007D
Streptavidin Sepharose beads	GE Healthcare	Cat#17-5113-01
Seahorse XF base medium	Agilent	Cat#103334-100
Seahorse XFe96 FluxPak	Agilent	Cat#102601-100
pMD19 T-vector	TAKARA	Cat#3270
3,3′,5,5′-Tetramethylbenzidine (TMB) substrate	Abcam	Cat#ab171523
Stop solution for TMB Substrate	Abcam	Cat#ab171529
Critical commercial assays		
SuperScript III First-Strand Sythesis	Invitrogen	REF#18080-051
HieffTM qPCR SYBR® Green Master Mix (Low Rox Plus)	Yeasen	Cat#11202ES08
AllPrep DNA/RNA/Protein Mini Kit	QIAGEN	Cat#80004
NextSeq® 500/550 High Output v2.5(150 Cycles)	Illumina	Cat#20024907
MicroPlex Library Preparation Kit v2	Diagenode	Cat#C05010012
TruSeq Stranded Total RNA (RiboZero Human/Mouse/Rat) Library Prep	Illumina	Cat#RS-122-2201
Deposited data		
All deposited data superseries	This study	GSE164072; https://www.ncbi.nlm.nih.gov/geo/query/acc.cgi?acc=GSE164072
ChIP-seq H4K5ac and H4K5cr (REH WT and KO)	This study	GSE164016
ChIP-seq BRD4 (REH WT and KO)	This study	GSE164031
RNA-seq REH WT and *FASTKD1* KO	This study	GSE164043
RNA-seq REH WT ctrl and JQ1	This study	GSE164045
RNA-seq B-ALL (25 patients)	This study	GSE164060
RNA-seq REH control and *FASTKD1* sh (knock down)	This study	GSE164071
Original western blot images	This study	Mendeley https://doi.org/10.17632/2hk6dhmcbr.1
Experimental models: Cell lines		
Human: acute lymphoblastic leukemia cell line REH	ATCC	CRL-8286; RRID: CVCL_1650
Human: acute lymphoblastic leukemia cell line REH depleted of *FASTKD1 (ko-1)*	This study	N/A
Human: acute lymphoblastic leukemia cell line REH depleted of *FASTKD1 (ko-2)*	This study	N/A
Cercopithecus aethiops: SV40 transformed kidney fibroblast cell line COS-7	ATCC	CRL-1651; RRID: CVCL_0224
Oligonucleotides		
sgRNA targeting sequences: *FASTKD1* #1: GTTATCTTCAACAACTCTAA	Sanjana et al., 2014	N/A
sgRNA targeting sequences: *FASTKD1* #2: AAATAGCTGATATTGTTCAT	Sanjana et al., 2014	N/A

(*Continued on next page*)

Continued

REAGENT or RESOURCE	SOURCE	IDENTIFIER
shRNA targeting sequences: *FASTKD1* #1: ACTTGCGTGCAACATCTTAAT	This study	N/A
shRNA targeting sequences: *FASTKD1* #2: GTCGGTTCTTACGCCTTATTAC	This study	N/A
shRNA targeting sequences: *FASTKD1* #3: GCCAGTTTGAATGGAACTCTAT	This study	N/A
shRNA targeting sequences: *FASTKD1* #4: GCTTCGTCTAAGAGCTATTTG	This study	N/A
shRNA targeting sequences: *FASTKD1* #5: ATTCGTCCATTCAGCGTATTG	This study	N/A
Primers see table S5	This study	N/A
Recombinant DNA		
Plasmid: lentiGuide-Puro	Kind gift from Feng Zhang (Sanjana et al., 2014)	Addgene plasmid # 52963; RRID: Addgene_52963
Plasmid: lentiCas9-Blast	Kind gift from Feng Zhang (Sanjana et al., 2014)	Addgene plasmid # 52962; RRID: Addgene_529 62
Plasmid: LeGO-iG2	Kind gift from Boris Fehse (Weber et al., 2008)	Addgene plasmid # 27341; RRID: Addgene_27341
Plasmid: LeGO-FASTKD1-3xflag	This study	N/A
Plasmid: Co1491-IRES-RFP	This study, kindly provided by Corinne Albiges-Rizo	N/A
Plasmid: Co1491-NLS-CobB-HA	This study, primary CMV-NLS-CobB construct is a kind gift from Heinz Neumann (Spinck et al., 2020)	N/A
Plasmid: pLVX-shRNA1	Clontech	Cat#632177
Plasmid: BRD4-NUT-GFP	Reynoird et al., 2010	N/A
Plasmid: pMD2.G	Kind gift from Didier Trono	Addgene plasmid #12259; RRID: Addgene_12259
Plasmid: psPAX2	Kind gift from Didier Trono	Addgene plasmid #12260; RRID: Addgene_12260
Plasmid: pRSV-Rev	Kind gift from Didier Trono (Dull et al., 1998)	Addgene plasmid # 12253; RRID: Addgene_12253
Software and algorithms		
STAR v2.5.2b	Dobin et al., 2013	https://github.com/alexdobin/STAR
Bowtie2 aligner	Langmead and Salzberg, 2012	http://bowtie-bio.sourceforge.net/bowtie2/index.shtml
DeepTools2	Ramírez et al., 2016	https://deeptools.readthedocs.io/en/develop/
R package DEseq2	Bioconductor	http://bioconductor.org/packages/3.12/bioc/html/DESeq2.html
HTseq v0.9.1	Anders et al., 2015	https://htseq.readthedocs.io/en/master/
Mascot v2.3.01	Matrix Science	http://www.matrixscience.com
Qual Browser v3.0.63	Thermo Fisher	N/A
ImageJ	Schneider et al., 2012	https://imagej.nih.gov/ij/
GraphPad Prism 5	Graphpad	http://bowtie-bio.sourceforge.net/bowtie2/index.shtml
ZEISS ZEN lite	ZEISS	https://www.zeiss.com/microscopy/int/products/microscope-software/zen-lite.html
SPSS Statistics v20	IBM	https://www.ibm.com/support/pages/downloading-ibm-spss-statistics-20

RESOURCE AVAILABILITY

Lead contact

Further information and requests for resources and reagents should be directed to and will be fulfilled by the Lead Contact, Saadi Khochbin (saadi.khochbin@univ-grenoble-alpes.fr).

Materials availability

Plasmids and cell lines generated in this study are available upon request.

Data and code availability

- The ChIP-seq data and RNA-seq data generated during this study haven been deposited at GEO and are publicly available as of the date of publication. Accession numbers are listed in the Key resources table. Original western blot images have been deposited at Mendeley and are publicly available. The DOI is listed in the Key resources table. Microscopy data reported in this paper will be shared by the lead contact upon request.
- This study does not report unpublished custom code, software or algorithms.
- Any additional information required to reanalyse the data reported in this paper is available from the lead contact upon request.

EXPERIMENTAL MODEL AND SUBJECT DETAILS

Cell lines and cell cultures

Human lymphoblastic leukemia cell line REH (Female, CVCL_1650) was obtained from National Collection of Authenticated Cell Cultures and was authenticated by STR analysis prior to use. REH and the derivative cells were maintained in RPMI-1640 (GIBCO) supplemented with 10% FBS (Dominique DUTSCHER), 4mM L-glutamine (GIBCO) and 1% Penicillin-Streptomycin (GIBCO). COS-7 (Male, CVCL_0224) were purchased from ATCC, and were cultured in DMEM (Low glucose, 1g/L, GIBCO) supplemented with 10% FBS, 4mM L-glutamine and 1% Penicillin-Streptomycin. All cells were incubated at 37°C with 5% CO_2.

CRISPR/Cas9 mediated knockout cell line

REH cells were co-introduced with lenti-Cas9 and lenti-sgRNAs plasmids (targeting sequences indicated in Key resources table) using the lentivirus infection approach described in the method details. 3 days after infection, positive cells with sgRNAs were enriched using 1.0 μg/ml puromycin (Sigma-Aldrich, Cat# P8833). Genotypes of the resultant cell populations were analyzed by PCR amplification (primers shown in Table S5) and sanger sequencing. Successful genome-editing of cell populations was documented by multi-spikes in the sequence map of PCR products. After being seeded into 96-well plates for 2-3 weeks, single cell clones were obtained and genotypes of each allele of single cell clones was analyzed through sanger sequencing following TA cloning of PCR products. Knockout clones with frameshift indels within the exons were used for further experiments.

B-ALL patients' bone marrow samples

All the patients (n = 31) enrolled in this study were newly diagnosed in Ruijin hospital (See Table S4). Bone marrow aspiration was conducted at diagnosis. Mononuclear cells were enriched from BM samples by density gradient centrifugation with LymphoPrep Solution (Axis Shield PoC, Cat#1114547) and were stored at −80°C as dry pellets for further experimental analysis. This study was approved by the ethical board of Shanghai Institute of Hematology. All patients and their guardians were provided with informed consent for sample collection and research in agreement with the Declaration of Helsinki.

METHOD DETAILS

Drug treatment and sample preparations

For sodium octanoate (Sigma-Aldrich, Cat#C5038) treatment, 5 x10^5/ml REH cells were seeded into 6-well plates, treated with or without indicated concentrations of sodium octanoate for 24 hours. For other compounds, REH wild-type, ko-1 and ko-2 cells were seeded at the density of 7.5 x10^5/ml in 6-well plates. Treatment strategy was as following: 100 nM ND-630 (MedChemExpress, Cat#HY-16901) for 6 hours, 0.5 μM Rotenone (Sigma-Aldrich, Cat#R8875) for 1 and 2 hours respectively, 0.5 mM Ranolazine (Sigma-Aldrich, Cat#R6152) for 6 hours, 3 μM Triascin C (Sigma-Aldrich, Cat#T4540) for 16 hours. After exposition to the different compounds, these cells were lysed with 8 M urea and subjected to sonication (Biorupter, High, 30 s ON/OFF, total 10min) to obtain total protein. Protein solutions were quantified using Bradford assay (Bio-rad) before being added with SDS-PAGE loading buffer for western blot analysis.

For JQ1 treatment, REH wild-type cells were exposed to 0.1 μM or 0.5 μM JQ1 or DMSO as control respectively for 24 hours. 5x10^6 cells were then harvested and yielded to RNA extraction with 500 μL TRIzol reagent (Invitrogen, Cat#15596018) according to the provider's protocol. Precipitated RNA was dissolved in DEPC-treated water and used for RNA-sequencing.

For salt elution experiments around $1x10^7$ REH wild-type, ko-1 and ko-2 or $4x10^6$ COS-7 control and CobB-ha expressing cells were harvested, washed twice with ice cold PBS, and split into equal aliquots. Each aliquot of cells was lysed in LSDB lysis buffer (50mM HEPES pH7.0, 3mM MgCl2, 20% glycerol, 0.1% NP-40, 1mM DTT, 1xprotease cocktail inhibitors) containing different concentrations of salts and 10mM sodium butyrate for 30 min on ice. For REH cells, the KCl concentrations of 100, 150, 200 or 250 mM were respectively used and for COS-7 cells, the KCl concentrations of 100, 150, 200 mM KCl were respectively added to the lysis buffer. After centrifugation at 12000 g 4°C for 10min, the supernatants were saved to detect soluble BRD4, while the nuclei pellets were subjected to SDS-PAGE loading buffer to detect chromatin tightly bound BRD4.

For JQ1 treatment assay correlated with Figure 4C, lower panel, $1x10^6$ /ml REH wild-type, ko-1 and ko-2 cells were exposed to 0.1 μM, 0.5 μM or 5 μM JQ1 or DMSO as control in 6-well plates. After 3 hours, cells were collected and lysed in LSDB lysis buffer with 100 mM KCl and 10 mM sodium butyrate for 30 min on ice. After centrifugation at 12000 g for 10 min at 4°C, supernatants were collected to detect soluble BRD4, while the nuclei pellets were subjected to SDS-PAGE loading buffer to detect chromatin tightly bound BRD4.

Plasmids, shRNA and sgRNA

FASTKD1 (NM_024622) was chemically synthesized and was cloned into LeGO-iG2 (Addegene #27341) vector to generate LeGO-*FASTKD1-3x Flag* construct. Co1491-IRES-RFP modified from pSicoR PGK (Addgene #12084) was kindly provided by Corinne Albiges-Rizo. Co1491-NLS-CobB-HA was subcloned from CMV-NLS-CobB, which was kindly provided by Heinz Neumann (Spinck et al., 2020). shRNAs and sgRNAs were designed using GPP Web Portal (https://portals.broadinstitute.org) or referring to GeCKO v2 library (Sanjana et al., 2014) with the corresponding targeting sequences indicated in the Key resources table, and were cloned into pLVX-shRNA1 (Clontech, Cat#632177) and LentiGuide-Puro plasmid (Addgene plasmid#52963) respectively. All plasmids were confirmed by sanger sequencing before being used in this study.

Lentivirus production and infection

5 μg lentiviral transfer and package plasmids were co-transfected into 293T cells in each well of 6-well plates using lipofectamine 2000 (Invitrogen, Cat#11668019) according to the manufacturer's instructions. For pLVX-shRNA1, lentiCas9-blast, lentiGuide-Puro and the derivative plasmids, second generation packaging plasmids (psPAX2 and pMD2G) were used for generating viral particles, and an additional pRSV-Rev plasmid was used for transferring LeGO-iG2 and Co1491-IRES-RFP backbone as well as the subcloned plasmids. Virus supernatants were collected at 24 and 48 hours after plasmid transfection and precleared with 0.45 μm filter (Millipore). Amicon Ultra-15 fiters (Millipore) were used to concentrate virus supernatants by centrifugation at 4000 rpm 4°C for 30 min. Concentrated virus was diluted with complete growth medium and immediately used to infect the cells of interests. Infection was performed in 12-well plates, with each well containing 1ml diluted virus medium and $2x10^5$ REH cells, or at 20% confluency in the case of COS-7 cells. 24 hours after infection, virus medium was washed out and replaced with fresh culture medium. Cells were then maintained regularly before further selection. For shRNA knockdown, positive cells were enriched 3 days after virus infection by 1.0 μg/ml puromycin treatment and were maintained for an average of 1 week before experimental analysis. For CobB and FASTKD1 re-expressing cells, RFP and GFP positive cells were respectively sorted with FacsAria IIu- cell sorter (BD Biosciences) 1-2 weeks after infection.

Histone preparation

Histone samples were prepared by acid extraction protocol as previously described with minor modifications (Buchou et al., 2017). In brief, $1x10^7$ REH wild-type, ko-1 and ko-2 cells, or $1x10^7$ COS-7 control and CobB expressing cells were lysed in 1 mL lysis buffer (0.06% NP-40, 10 mM HEPES pH 7.0, 10 mM KCl, 1.5 mM $MgCl_2$, 0.34 M sucrose, 1xprotease cocktail inhibitor) with 10 mM sodium butyrate for 10 min on ice. Cell nuclei were pelleted by centrifugation at 250 g 4°C for 5 min, and subjected to histones extraction using 0.2 M H_2SO_4 for 16 hours at 4°C. After centrifugation at 16000 g for 10 min at 4°C, solubilized histones were collected and then precipitated by adding TCA drop by drop to the final volume of 20%. Histone pellets were then washed once with cold acetone + 0.1%HCl, twice with cold acetone and were dried completely in air.

MS quantification of histone acylations

5 μg of each histone sample from REH wild-type, ko-1 and ko-2 cells were separated by SDS-PAGE and each spliced histone band was in-gel digested with trypsin. The tryptic peptides were analyzed by Orbitrap Fusion following an EASY-nLC 1000 HPLC system (Thermo Fisher Scientific, San Jose, CA). Mass spectrometry data were analyzed by Mascot software (version 2.3.01, Matrix Science Ltd., London, UK) against an in-house human histone sequence database (83 sequences; 13,870 residues) generated from the UniProt database (updated on 01/27/2015). All identified MS/MS spectra were manually verified. Peptides containing modifications were manually quantified using the Qual Browser (version 3.0.63, Thermo Fisher Scientific, San Jose, CA) by the area under the curve (AUC) of the extracted precursor ion of each peptide. Acylated histone peptides were normalized to the corresponding histone peptides. The relative abundance of indicated histone acylations in two *ko* clones versus wild-type cells was plotted in the column chart.

Peptide pull-down assay

Peptides pull-down assay was performed using a protocol described previously (Goudarzi et al., 2016). Briefly, peptides (H4 /H4K5acK8ac /H4K5buK8bu /H4K5acK8bu /H4K5buK8ac /H4K5bu /H4K8bu) were first bound to beads by incubating equal amount

of each type of peptide with Streptavidin Sepharose beads (GE Healthcare, Cat#17-5113-01) in PBS supplemented with 100ng/ml TSA for 20min. Bound beads were then washed with PBS and LSDB lysis buffer (50 mM HEPES pH 7.0, 3 mM $MgCl_2$, 20% glycerol, 0.1% NP-40, 1 mM DTT, 1xprotease cocktail inhibitors) with 25mM KCl and 10mM sodium butyrate.

Around $1x10^7$ *FASTKD1 ko* or wild-type cells were harvested and lysed in 500 μL LSDB lysis buffer with 500 mM KCl and 10 mM sodium butyrate for 20 min on ice. After centrifugation at 12000 g for 10 min at 4°C, protein supernatants were collected and diluted with LSDB lysis buffer with 10 mM sodium butyrate to achieve the salt concentration of 250 mM. A small volume of diluted protein supernatants was saved for input, and the rest was split into equal aliquots, each incubated with the corresponding conjugated beads for 2 hours at 4°C. Beads then were pelleted and washed twice with LSDB lysis buffer with 250mM KCl and 10 mM sodium butyrate and once with PBS with 10 mM sodium butyrate. After incubating with 1x SDS-PAGE loading buffer at 100°C for 5min, pulled-down complexes were eluted from beads and preserved for western blotting analysis.

Western blotting

Western blotting with SDS-PAGE were carried out according to standard procedures using the antibodies listed in Key resources table. After adding ECL substrates (Bio-rad), revelation was performed with Chemidoc (Bio-rad) or Vilber Chemiluminescence system (Vilber). The dilutions of antibodies used in this study are as follows: anti-BRD4 (Bethyl Lab, 1:2000), anti-H4K5bu (PTM biolabs, 1:1000), anti-H4K8bu (PTM biolabs, 1:1000), anti-H4K5cr (PTM biolabs, 1:1000), anti-H4K8cr (PTM biolabs, 1:1000), anti-H4K5ac (PTM biolabs, 1:1000), anti-H4K8ac (PTM biolabs, 1:1000), anti-H4K5bhb (PTM biolabs, 1:1000), anti-H4K5lac (PTM biolabs, 1:1000), anti-HA (Abcam, 1:2000), anti-H4 (Abcam 1:1000), Anti-β-Actin (Sigma-Aldrich, 1:5000), Goat anti Rabbit IgG(H + L)-HRP (Bio-rad, 1:5000), Goat anti-Mouse IgG (H + L)-HRP (Bio-rad, 1:10000).

Relative quantification of histone acylations with ELISA

Indirect ELISA was set up according to a protocol described previously (Dai et al., 2011). Total protein was obtained from $5x10^6$ mononuclear cells of each patient in parallel with RNA extraction using AllPrep DNA/RNA/Protein Mini Kit (QIAGEN) following the manufacturer's instructions. In the case of COS-7 control and CobB expressing cells, histones prepared through acid extraction protocol were used for ELISA assay. These precipitated proteins were dissolved in a small volume of 8 M urea and quantified by Bradford reagent (Bio-rad). Protein solution was diluted with PBS and coated into triplicate wells of 96-well flat-bottom plates (Nunc-Immuno products, Thermo Fisher) at 4°C for 16 hours. The amount of protein being coated was optimized according to the histone marks being detected and the protein samples being used. In the case of total protein of B-ALL patients' samples, the protein amount for each well was as follows: 2.5 μg for H4K5cr and H4K5bu detection, 0.0125 μg for H3 detection. In the case of protein from COS-7 control and CobB expressing cells, the amount of protein for each well was as follows: 0.15 μg for H4K5bu and H4K5ac detection, 0.3 μg for H4K5cr detection, 0.015 μg for H4 detection. Coated plates were then blocked with 5% BSA for 1 hour at room temperature and sequentially incubated with primary antibodies accordingly and secondary antibodies. Dilutions of the antibodies used in this assay were: H4K5cr (PTM biolabs, 1:500), H4K5bu (PTM biolabs, 1:500), H3 (Abcam,1:5000), H4K5ac (Abcam, 1:2000), H4 (Abcam, 1:1000), HRP linked Goat anti Rabbit IgG (Bio-rad or CST, 1:4000). After the addition of TMB substrate (Abcam, Cat#ab171523) and acid stop solution (Abcam, Cat#ab171529), the signal intensity was recorded at OD 450 nm. Relative quantity of histone marks was calculated based on the value of signal intensity.

Immunofluorescence

Empty vector and FASTKD1-Flag expressing cells were treated with 250 nM Mitotracker Red (Invitrogen, Cat#M7512) dye for 20 min at 37°C in CO2 incubator. Approximately $8x10^4$ cells were then collected, washed once with PBS and spined onto glass slide at 800 rpm for 5 min. Fixation was performed using 4% paraformaldehyde for 15 min, followed by permeabilization with 0.3% Triton X-100 for 10 min at room temperature. After being blocked with 10% BSA for 1 hour at room temperature, slides were sequentially incubated with anti-Flag antibody (Sigma-Aldrich, 1:500 dilution) and anti-Mouse IgG DyLight 405 (Invitrogen, 1:500 dilution). Fluorescent images were captured by confocal laser scanning microscope (TCS SP8, Leica) under a 63x 1.40 numeric aperture oil-immersion lens and were processed with ImageJ.

Fluorescence recovery after photobleaching (FRAP)

$2x10^5$ COS-7 control and CobB expressing cells were seeded in 1-well Chambered Coverglass (LAB-TEK brand products, Thermo Fisher) respectively the day before being transfected with 1 μg BRD4-NUT-GFP plasmid using lipofectamine 2000 (Invitrogen). 24 hours after transfection, FRAP was performed on 8 independent cells of each group using fluorescent microscope (LSM710 NLO-LIVE7-Confocor3, Zeiss) equipped with a 488 nm laser and a LP505 filter. A circular region on GFP foci was bleached for 1.592 s and the recovery of fluorescence was recorded each second for a duration of 75 s after photobleaching by software ZEN lite. Immunofluorescence photos of BRD4-NUT-GFP foci from control and CobB expressing cells were captured before FRAP.

For the data analysis and plotting, fluorescence intensity was normalized and rescaled to a reference axis from 0 to 1. 8 datasets from each cell group were individually fitted using the single exponential model: $I(t) = \alpha\left(1 - 2^{-\frac{t}{\kappa}}\right)$. The 8 biological replicates giving

the best fitting statistics were used to calculate the average half-life ($t_{1/2}$) of fluorescence recovery (κ) and average mobile fractions (α). Values of mean ± 2 SEM are shown in the figure. FRAP curve was plotted on the mean of the 8 biological replicates ± 2 SEM at each time point.

Metabolic assay

Metabolic assay was performed according to the Seahorse XF Cell Mito Stress Test user manuals. Briefly, 1 × 10^5 REH wild-type, ko-1 and ko-2 cells were resuspended in 180 μL assay medium formulated as pH 7.4 ± 0.1 bicarbonate-free Seahorse XF base medium (Agilent, Cat#103334-100), with 10 mM glucose (GIBCO), 1 mM sodium pyruvate (GIBCO) and 4 mM L-glutamine (GIBCO). Resuspended cells were then seeded in XF96 cell culture plates (Agilent, Cat#102601-100), which had previously been coated with 0.1% gelatin (Sigma-Aldrich, Cat#G1393) for at least 1 hour at room temperature. The seeded plates were then incubated at 37°C for 1 hour in a non-CO2 incubator before being loaded onto Seahorse XFe96 Analyzer (Agilent). Oxygen consumption rate (OCR) was measured at basal level as well as after injection of 1 μM oligomycin A (Sigma-Aldrich, Cat#75351), 1 μM FCCP (Sigma-Aldrich, Cat#C2920), 0.5 μM rotenone (Sigma-Aldrich, Cat#R8875) and 1 μM antimycin A (Sigma-Aldrich, Cat#A8674). OCR values (pmol/min) were normalized to cell number. Mean ± SEM based on 5 replicates were plotted in the figure.

RT-qPCR

5x10^6 cells from *FASTKD1* wild-type and two *ko* clones, or from shCtl and two shRNAs knockdown cell lines were collected and lysed in 500 μL TRIzol reagent (Invitrogen, Cat#15596018). Total RNA was obtained by phenol-chloroform extraction and isopropanol precipitation using standard procedure. For B-ALL patients' samples, total RNA was extracted from 5x10^6 mononuclear cells of each patient using AllPrep DNA/RNA/Protein Mini Kit (QIAGEN, Cat# 80004) following the manufacturer's instructions.

cDNA was produced from 1 μg RNA with superscript III transcriptase (Invitrogen, Cat#18080-051) using random hexamers according to the manufacturer's instructions. Quantitative PCR (qPCR) was performed with SYBR green reagent (Yeasen, Cat#11202ES08) on ViiA 7(The Applied Biosystem) using primers described in Table S5. *CPT1A* and *ND2* with patients' samples were calculated via -dCt against GAPDH. The correlation between *CPT1A* and *ND2* was analyzed with Spearman correlation. Mean values of triplicates were plotted with scatterplot using GraphPad Prism 5. Fold changes of gene expression levels were calculated via 2^-ddCt and are represented by mean ± SEM based on at least three independent experiments. Statistical differences between wild-type and two *ko*, or between shCtl and shRNAs groups were calculated with Fisher's Least Significant Difference (LSD) post one-way ANOVA test. * $p < 0.05$, ** $p < 0.01$, ***$p < 0.001$.

RNA-seq

Three independent RNA extractions from *FASTKD1* wild-type and two *ko* clones (ko-1, ko-2), or from control and two knockdown cell lines (sh-1, sh-2), or from solvent and JQ1 treated wild-type cells, or from 25 B-ALL patients' bone marrow samples were sequenced. For each sample, 1 μg RNA samples (RIN = 10) were used for libraries preparations with TruSeq Stranded Total RNA (RiboZero Human/Mouse/Rat) Library Prep (Illumina, Cat#RS-122-2201) according to manufacturer's instructions. Each library was quantified on Qubit with Qubit® dsDNA HS Assay Kit (Life Technologies) and the size distribution was examined on the Fragment Analyzer with High Sensitivity NGS Fragment Analysis kit (Agilent). Libraries prepared from solvent and JQ1 treated cells samples were sequenced on Illumina NS500 (PE75) at the TGML Platform of Aix-Marseille Université, and those prepared from *FASTKD1* control and knockdown, wild-type and knockout cells samples, and B-ALL patients' samples were sequenced on Hiseq 4000 (PE150) platform in Novagene company.

The sequenced reads were aligned from raw sequence fastq data using STAR v2.5.2b software on UCSC hg19 reference genome. The aligned reads were normalized, and log transformed using the R bioconductor package DEseq2 (http://bioconductor.org/packages/3.12/bioc/html/DESeq2.html).

The standardized and normalized read counts of mitochondrial genes were used to generate a heatmap in Figure 1A. Supervised transcriptomic analyses were performed to identify genes significantly up-and downregulated between two conditions using thresholds of Student t test p value < 0.05 and fold change absolute value of 1.5.

ChIP-seq

ChIP assays for H4K5cr, H4K5bu, H4K5ac and BRD4 were carried out as previously described with minor modifications (Buchou et al., 2017, Barral et al., 2017). Around 5 −10 x10^7 REH wild-type, ko-1 and ko-2 cells were harvested and lysed in 1.5 mL lysis buffer (0.05% Triton X-100, 15 mM Tris-HCl pH 7.4, 60 mM KCl, 15 mM NaCl, 0.34 M sucrose, 2 mM EDTA, 0.5 mM EGTA, 1 mM DTT, 0.65 mM spermidine, 1x protease cocktail inhibitors) with 10 mM sodium butyrate and incubated for 5 minutes at 4°C. Cell nuclei were pelleted by centrifugation at 250 g for 5 min at 4°C and resuspended in MNase buffer (10 mM Tris-HCl pH 7.5, 10 mM KCl, 2 mM $CaCl_2$) with10 mM sodium butyrate. Then the cell nuclei solution was subjected to micrococcal nuclease S7 (Sigma-Aldrich, Cat#10107921001) digestion (5U MNase per 100 μg nuclei) at 37°C for 20 min to obtain mononucleosomes. Small aliquots of mononucleosomes solutions were collected for input and used to check the efficiency of digestion before immunoprecipitation.

Immunoprecipitations were carried out as follows: 5 μg anti-H4K5cr (PTM biolabs, Cat#PTM-521), anti-H4K5bu (PTM biolabs, Cat#PTM-310), anti-H4K5ac (abcam, Cat#ab51997), anti-BRD4 (Bethyl lab, Cat#A301-985A100) antibodies were coupled with 50 μl Dynabeads protein G (Thermo Fisher, Cat#10007D) respectively according to the manufacturer's instructions. Digested

mononucleosomes solutions were diluted with LSDB500 buffer (50 mM HEPES pH 7.0, 3mM MgCl2, 500 mM KCl, 20% glycerol, protease cocktail inhibitors) with 10 mM sodium butyrate to achieve the final KCl concentration of 350 mM. For each reaction, around 100 μg chromatin was incubated with antibody-coupled beads at 4°C for 16 hours. Immunoprecipitated beads were then washed three times with LSDB350 buffer (50 mM HEPES pH 7.0, 3 mM $MgCl_2$, 350 mM KCl, 20% glycerol, protease cocktail inhibitors) with 10 mM sodium butyrate and one time with elution buffer (10 mM Tris-HCl pH 8.5, 1 mM EDTA). ChIP samples were eluted from beads with elution buffer containing 1%SDS at 65°C for 15 min and were purified by phenol-chloroform extraction and ethanol precipitation in parallel with input samples.

For sequencing, ChIP libraries were prepared using MicroPlex Library Preparation Kit v2 (Diagenode) according to manufacturer's instructions. Each library was quantified on Qubit with Qubit® dsDNA HS Assay Kit (Life Technologies) and size distribution was examined on the Fragment Analyzer with High Sensitivity NGS Fragment Analysis kit (Agilent).

ChIP libraries against H4K5cr, H4K5ac and BRD4 (1^{st} experiment) were sequenced on a High-output flow cell (400M clusters) using the NextSeq® 500/550 High Output v2.5 150 cycles kit (Illumina), in paired-end 75/75nt mode, according to manufacturer's instructions at the TGML Platform of Aix-Marseille University.

ChIP libraries against H4K5bu and BRD4 (2^{nd} experiment) were sequenced using the NovaSeq 6000 in PE150 mode according to manufacturer's instructions at the Novogene company.

Raw fastq files were processed by 5 prime trimming, keeping 30 bp-length fragments, using 'fastx_trimmer' (with options -l 30 -Q33). The trimmed fastq files were aligned on the USCS human hg38 genome using the Bowtie2 aligner (Langmead and Salzberg, 2012), with options –end-to-end, –no-mixed, –no-discordant. The aligned reads were filtered according to alignment quality (mapping quality score > 30) and normalized using bamCoverage by Reads Per Kilobase per Million mapped reads (RPKM) for the anti K5ac, K5cr and Kbu ChIP-seq and scaling factors for the anti-BRD4 ChIP-seq.

For the anti-BRD4 ChIP-seq, scaling factors were computed according to the Spike in free method (Jin et al., 2020). Accordingly, for the first experiment, the respective scaling factors 4.25, 3.58 and 5.81 were applied when calculating the BRD4 ChIP-seq read coverage in wild-type, ko1 and ko2 cells. For the second experiment the corresponding scaling factors of 4.85, 4.6 and 5.72 were respectively applied.

The aligned read counts were converted into a 10 bp bin matrix of the signal 2Kb upstream and downstream genes TSS, using computeMatrix (from the package deepTools2, Ramírez et al., 2016), heatmaps and profiles were generated using the respective deepTools2 packages, plotHeatmap and plotProfile.

Script for bamCoverage normalizing with RPKM:

```
bamCoverage -b myfile_notrim.srt.bam–extendReads–binSize 4–minMappingQuality 30–normalizeUsing RPKM -o myfile_notrim.bw
Script for bamCoverage with scaling factors:
bamCoverage -b my_file.bam–extendReads–numberOfProcessors 4–binSize 4–minMappingQuality 30–normalizeUsing None–scaleFactor my_value -o my_file.bw
Scripts for computeMatrix and plotHeatmap
computeMatrix reference-point -R tss_grch38.bed -S ＼
file1.bw ＼
file2.bw ＼
…
–outFileName matrix_tss_grch38.txt.gz–referencePoint TSS–binSize 10–beforeRegionStartLength 2000–afterRegionStartLength 2000–numberOfProcessors 32–sortRegions keep
plotHeatmap–matrixFile matrix_tss_grch38.txt.gz–outFileName hm_tss_grch38.png–colorMap YlOrRd–sortRegions descend
```

QUANTIFICATION AND STATISTICAL ANALYSIS

Statistical analysis was performed with SPSS v20. Details of the number and type of replication for each experiment were described in method details or figure legends where appropriate. Each dot represents one individual in patients' experiment. Data were presented as median with interquartile range for non-normally distributed populations of patients' samples or mean ± 2 standard error of the mean (SEM) for FRAP experiment. All other data were presented as mean ± SEM. When comparing normally distributed two groups, statistical significance was determined by Student t test. When comparing multiple groups, Fisher's LSD post one-way ANOVA test was used to determine the significance between groups. When comparing non-normally distributed data, Mann-Whitney U test was used to determine the significance, and Spearman correlation was used to determine the correlation. $p < 0.05$ were considered statistically significant. Statistics are *$p < 0.05$, **$p < 0.01$, ***$p < 0.001$.